Supplementary Information for

Source-dependent wet scavenging of char and soot at a regional background site of the Yangtze River Delta region, China

Changliu Wu[1,2,3], Fang Cao[1,2,3*], Feng Xie[1,2,3], Yuxian Zhang[1,2,3], Xiaoying Yang[1,2,3], Wenhuai Song[1,2,3], Mingyuan Yu[1,2,3], Qianli Ma[4], Yuan Dai[2,5], Xiaofang Jia[6], Sönke Szidat[7], and Yanlin Zhang[1,2,3]

[1]School of Ecology and Applied Meteorology, Nanjing University of Information Science and Technology, Nanjing 210044, China.

[2]Jiangsu Key Laboratory of Intelligent Atmospheric Environment Monitoring and Carbon-Pollution Co-control, Nanjing University of Information Science and Technology, Nanjing 210044, China.

[3]State Key Laboratory of Climate System Prediction and Risk Management, Nanjing University of Information Science and Technology, Nanjing 210044, China.

[4]Zhejiang Lin'an, Atmospheric Background, National Observation and Research Station, Hangzhou 311300, China.

[5]Yangzhou Environmental Monitoring Center, Department of Ecology and Environment of Jiangsu Province, Yangzhou 225009, China.

[6]Meteorological Observation Center, China Meteorological Administration, Beijing 100081, China.

[7]Oeschger Centre for Climate Change Research, University of Bern, Bern 3012, Switzerland.

***Corresponding author:** Fang Cao (caofangle@163.com)

Contents of this file

49 pages, 4 texts, 13 tables, and 22 figures

Text S1 Analytical methods of various chemical tracers

(1) Water-soluble inorganic ions

Water-soluble inorganic ions measured using an ion chromatograph (ICS 5000+, Thermo Scientific). Certain amounts of filters were placed into the Teflon bottles, sealed with 5 mL of ultrapure water (Milli-Q Reference, USA), sonicated for 30 minutes, and filtered through a 0.22 μm aqueous-phase needle filter for analysis. The cations and anions were determined by system I (guard column: CG12A 4 mm; separation column: CS12A 4 mm) and system II (guard column: AG11 HC 4 mm; separation column: AS11 HC 4 mm), respectively.

(2) Total metal and metalloid elements

An appropriate quantity of the sample was obtained using a cutter and added into the digestion tube. Subsequently, 5 mL of HNO_3 (GR) was utilized for the microwave digestion of particulate matter employing a high flux microwave digestion device (Mars-6, CEM, USA). The digestion process was configured to gradually heat up for 20 minutes to 170℃ and maintain at 170℃ for 30 minutes. After cooling to room temperature, an adequate amount of ultrapure water was added to soak the particles. The dissolved sample suspension was filtered into a centrifuge tube using a disposable syringe equipped with a 0.22μm aqueous phase needle filter, and then filled with ultra-pure water to 50 mL, and stored at 4℃ for measurement.

The metal and metalloid elements in the samples were determined by the inductively coupled plasma mass spectrometer (ICP-MS, iCAP RQ, Thermo Scientific, USA) at the Yangzhou Environmental Monitoring Center, Department of Ecology and Environment of Jiangsu Province. The internal standard method was adopted to quantify the target element, and the internal standard was Rhodium (^{103}Rh). The standard solution of gradient concentration was determined prior to sample testing and the standard curve was established. The correlation of the standard curve achieved 0.999 after sample testing. During the sample testing process, the process blank and the environment blank were corrected accordingly. For every 24 samples, one parallel sample and one mixed standard sample containing all target elements were determined. The standard deviation of parallel samples was less than 15%, which fulfilled the requirements of quantitative analysis of organic matter. In this study, a total of 10 elements such as V, Cr, Mn, Ni, Cu, Zn, AS, Cd, Ba and Pb were detected.

(3) Polar and non-polar organic molecular tracers

The organic compounds were determined by gas chromatography-mass spectrometry

(GC-MS) system (*GC7890B/MS5977A, Agilent Technologies; Santa Clara, CA*). Polar organic compounds were analyzed following a series of procedures, including extraction, filtration, concentration, and derivatization. Briefly, a 0.5024 cm^2 aliquot of the filter sample was extracted with a mixture of dichloromethane and methanol (2:1, v/v). The solvent extracts were filtered and concentrated via a vacuum rotary evaporator. To derivatize the extracts, 50 μL of *N, O*-bis-(trimethylsilyl) trifluoroacetamide (BSTFA) with 1% trimethylsilyl chloride and 10 μL of pyridine were added and incubated at 75°C for 3 hours. The derivatives were then diluted with 40 μL of internal standard (C_{13} n-alkane, 1.43 $ng \cdot \mu L^{-1}$) and analyzed by GC-MS. Non-polar organic compounds, including n-alkanes, polycyclic aromatic hydrocarbons (PAHs), hopanes, and steranes, were separated and detected using a linked thermal desorption (TD) system coupled with GC-MS. A 0.53 cm^2 piece of filter sample was placed into a TD quartz tube (80 mm length × 3 mm inner diameter), and 1 μL of an internal standard mixture, consisting of hexamethylbenzene and four deuterated compounds, was injected and analyzed by GC-MS.

Method blanks, field blanks, recovery experiments, and the determination of parallel samples were used for quality control and assurance. Recovery experiments were conducted by dripping 1μg of the mixed-standard solution on the blank filter (n=3) and then analyzing it as sampled filters. The recoveries of all standards were between 70% and 130% and the linear correlation coefficients (R^2) of all standard curves reached 99.9% at least. The blank filters (n=3) and field blank filters (n=8) were analyzed by the same procedures as sampled filters, in which target organic components were not detected.

(4) Determination of the ^{14}C of TC

The ^{14}C measurement was conducted in the Laboratory for the Analysis of Radiocarbon (LARA), University of Bern, Switzerland. Briefly, a 1.5 cm^2 punch from the filter sample was taken for burning under pure O_2 (99.9995 %) at 870℃ with thermos-optic OC/EC analyzer (*Model 5L, Sunset Laboratory Inc., USA*) for 240s to completely convert the carbon to CO_2 and then the ^{14}C in CO_2 was measured by using the tabletop accelerator mass spectrometry (AMS) system Mini Carbon Dating System (MICADAS) (Szidat et al., 2014). The ^{14}C content of the samples were expressed as the fraction of modern ($F_m{}^{14}C$), i.e. the $^{14}C/^{12}C$ ratio of the sample to the $^{14}C/^{12}C$ ratio of atmospheric CO_2 in the reference year 1950 (Stuiver and Polach, 1977):

$$F^{14}C=(^{14}C/^{12}C)_{sample}/(^{14}C/^{12}C)_{1950} \quad (S1)$$

Due to the nuclear bomb experiments in the 1950s and 1960s, the ^{14}C of CO_2 in the atmosphere has increased dramatically until 1963 and ^{14}C has decreased in the atmosphere since then (Xiong et al., 2021). To obtain accurate non-fossil fractions of TC ($f_{TC,nf}$), reference value ($f_{nf,ref}$) was calculated by pure contemporary carbon sources.

$$f_{nf}(TC)=\frac{F^{14}C(TC)}{f_{nf,\,ref}} \quad (S2)$$

The contemporary carbon sources including biogenic and biomass burning emissions ($f_{bio,ref}$ and $f_{bb,ref}$, respectively). In this study, the value of $f_{bb,ref}$ was estimated by tree growth models using 10-year-old, 20-year-old, 40-year-old, 70-year-old, and 85-year-old trees at scales of 0.2, 0.2, 0.4, 0.1, and 0.1, respectively (Mohn et al., 2008). The value of $f_{bio,ref}$ was obtained from ^{14}C measurements in atmospheric CO_2 recorded in the annual rings of tree in Qinghai Province, China, by Xiong et al. (2021). The living-plant-derived $f_{bio,ref}$ after 2015 was obtained from the simulation calculation of ^{14}C of recorded CO_2 by Xiong et al. (2021). The $f_{bb,ref}$ for 2020 was 1.104±0.06 and $f_{bio,ref}$ was 1.005 ± 0.05. Therefore, the upper and middle values of the $f_{nf,ref}$ were determined as $f_{bb,ref}$ (1.104) and $f_{bio,ref}$ (1.005).

$$TC_{nf} = TC \times f_{nf}(TC) \quad (S3)$$

$$TC_{ff}=1-TC_{nf} \quad (S4)$$

TC was apportioned into non-fossil sources (TC_{nf}) and fossil fuel sources (TC_{ff}).

Text S2 Source apportionment based on Latin Hypercube sampling (LHS) method.

The contributions of major sources to carbonaceous aerosols are estimated based on LHS method incorporating the ^{14}C of total carbon ($^{14}C_{TC}$) and carbonaceous component (i.e. OC, EC and LG, as shown in the Table S1): fossil sources (OC_{ff} and EC_{ff}), primary biomass burning sources (POC_{bb} and EC_{bb}), and other non-fossil carbon formed ($OC_{other, nf}$).

Firstly, POC_{bb} is estimated by the LG concentrations and the ratio of $(OC/LG)_{bb}$:

$$POC_{bb}=LG\times\left(\frac{OC}{LG}\right)_{bb} \quad (S5)$$

However, the concentrations of LG multiplying the ratio of $(LG/OC)_{bb}$ can derive POC_{bb}, but the $(LG/OC)_{bb}$ values can vary highly with the change of the type of BB material and the conditions of burning thereby introducing the uncertainty (Hou et al., 2021; Song et al., 2022). To determine an appropriate $(LG/OC)_{bb}$ value, seasonal $(LG/OC)_{bb}$ ratios were inferred from certain types of biomass fuels based on the above ratios of LG/MN and MA/GA as well as other reported studies (Engling et al., 2009; Jung et al., 2014; Liang et al., 2021; Sang et al., 2013; Schmidl et al., 2008). The central value for $(LG/OC)_{bb}$ was set at 0.13, and the detailed information are displayed in Table S2.

And EC_{bb} is calculated by the POC_{bb} and $(EC/OC)_{bb}$:

$$EC_{bb}=POC_{bb}\times\left(\frac{EC}{OC}\right)_{bb}=LG\times\left(\frac{OC}{LG}\right)_{bb}\times\left(\frac{EC}{OC}\right)_{bb} \quad (S6)$$

then, EC_{ff} is calculated by the subtraction of EC_{bb} from EC:

$$EC_{ff}=EC-EC_{bb} \quad (S7)$$

and OC_{ff} is equal to TC_{ff} minus EC_{ff}:

$$OC_{ff}=TC_{ff}-EC_{ff} \quad (S8)$$

OC_{nf} is divided into POC_{bb} and the other non-fossil OC sources:

$$OC_{nf}=POC_{bb}+OC_{other,nf} \quad (S9)$$

The LHS method was executed by using MATLAB software to produce 3000 random simulated variables. And simulations that yielded negative outcomes were disregarded, and the median of the remaining simulations was selected as the most precise estimation. The range of uncertainty was characterized by the 10^{th} and 90^{th} percentiles of all solutions. In addition, a comparison between $F_m{}^{14}C_{EC}$ measurements by MICADAS and LHS-based reconstructed

values for $PM_{2.5}$ samples collected in Thailand in our previous study have shown a relatively low deviation of ~6.5% for $F_m{}^{14}C_{EC}$ (Song et al., 2022), as shown in Figure S1, indicating the validity of the LHS-based estimation.

Notably, only a portion of samples (n = 31) collected at Lin'an were tested for $^{14}C_{TC}$ in this study, and the LHS calculation was conducted with the constraint of $^{14}C_{TC}$, as shown in Figure S2 for the frequency distribution of the most precise estimation. To obtain the EC_{bb} (or EC_{ff}) fractions of the samples without the measurement of $^{14}C_{TC}$, therefore, a LHS-based correction curve of EC_{bb} fractions was established between the ^{14}C-constraint and the no-^{14}C-constraint, with a significant estimation performance (r^2 = 0.99, $p \leqslant 0.0001$), as shown in Figure S3. And a comparison between estimations under the ^{14}C-constraint and the no-^{14}C-constraint show a relatively low deviation of -3.98% ~ 4.17% for EC_{bb} fractions (Figure S4 and S5), indicating the rationality of the correction curve for the estimation based on characteristic endmembers.

Text S3 Positive matrix factorization (PMF) model

The PMF receptor model has been widely applied in source apportionment of atmospheric pollutants (Liang et al., 2016). It decomposes response data into key contributing factors and calculates the contribution of each factor. The model is formulated as follows:

$$x_{ij}=\sum_{k=1}^{p} g_{ik}f_{kj}+e_{ij} \quad \text{(S10)}$$

wherein, x_{ij} represents the concentration of element j in sample i, (i = 1, 2, …, n; j = 1, 2, …, m), g_{ik} denotes the contribution of source k to sample i, f_{kj} represents the content of element j in source k, and e_{ij} is the residual. The PMF model employs a weighted least squares method for iterative calculations, decomposing the matrix x repeatedly to minimize the objective function Q and obtain the optimal matrices g and f. The objective function Q is defined as:

$$Q=\sum_{i=1}^{n}\sum_{j=1}^{m}\left(\frac{x_{ij}-\sum_{k=1}^{p} g_{ik}f_{kj}}{u_{ij}}\right)^2=\sum_{i=1}^{n}\sum_{j=1}^{m}\left(\frac{e_{ij}}{u_{ij}}\right)^2 \quad \text{(S11)}$$

wherein, u_{ij} represents the uncertainty in the concentration of element j in sample i. The PMF model assigns weights to each individual data point, providing an appropriate level of uncertainty for each data entry. And the specific operational details in this study were as follows:

(1) Data input

The dataset input for the PMF model (with 129 samples) consists of the concentrations and uncertainties of various combustion sources/primary emission tracers in this study, including LHS-^{14}C-based EC_{bb}/EC_{ff}, anhydrosugars (biomass burning tracers), polycyclic aromatic hydrocarbons (fossil-related tracers), hopanes (fossil-related tracers), metals/metalloid elements (primary emission tracers), and water-soluble inorganic ions (Ca^{2+} and Mg^{2+} for dust sources; K^+ for biomass burning). Here, both BC and char were set as the total variable (i.e., select and click on the "weak" option in the EPA PMF 5.0 software) for source apportionment, and the concentrations of soot from various sources were obtained by subtracting the char concentrations from the corresponding BC concentrations. The uncertainties of all species were calculated based on the following Equation S12 according to the EPA PMF 5.0 User Guide:

$$\text{Uncertainty}=\sqrt{(\text{Error Fraction}\times\text{Concentration})^2+(0.5\times\text{MDL})^2} \quad \text{(S12)}$$

Wherein, *MDL* is the method detection limit of each specie, and the *MDL* dataset of various tracers were detailed in our previous study (Cao et al., 2021; Cao et al., 2024; Song et al., 2026; Xie et al., 2026; Yang et al., 2025).

(2) Determine the number of factors

In this study, the number of factors (ranging from 2 to 8) was set to 100 iterations (robust model), with random initial points selected for each run of the PMF model, resulting in converged solutions. The optimal setting of factor number was determined according to the variation characteristics of $Q_{true}/Q_{expection}$. Wherein, Q_{true} is the actual output value of the PMF model, and $Q_{expection}$ was calculated by the following Equation S13.

$$Q_{expection}=N_{sam.}\times N_{tra.}-N_{fac.}\times\left(N_{spe.}+N_{sam.}\right)\times\left(N_{spe.}\div N_{sam.}\right) \quad (S13)$$

Wherein, $N_{sam.}$, $N_{tra.}$, $N_{fac.}$, and $N_{spe.}$ represent the number of samples, chemical tracers, factors, all species input, respectively. As illustrated in Figure S6, transitioning from 2 to 3 factors and from 3 to 4 factors led to substantial reductions in the $Q_{true}/Q_{expection}$ ratio, with decreases of 0.56 and 0.33, respectively; in contrast, the reductions were comparatively modest when increasing the number of factors from 4 to 5 (0.18) and from 5 to 6 (0.16). A decreasing trend in Q with an increasing number of factors may suggest overfitting, i.e., the inclusion of excessive factors that diminish model parsimony and generalizability (Brown et al., 2015), and the 4-factor solution consequently was the optimal solution.

(3) Uncertainty Estimation

To assess the robustness and uncertainty of the four-factor solution, both the displacement (DISP) and bootstrapping (BS) analyses were conducted. Following the EPA PMF 5.0 User Guide, the DISP intervals account for rotational ambiguity but exclude contributions from random measurement errors, and the BS intervals incorporate random errors and partially address rotational ambiguity. As summarized in Tables S3-S5 and Figure S7, the minimal rotational ambiguity in the four-factor solution supported the interpretability and reliability of the base model and its associated error estimates. The absence of factor swaps across all uncertainty runs, together with a low d_Q value, further confirmed that the solution was well-constrained.

Text S4 Uncertainty evaluation of the attenuation-derived apparent MAE calculation

According to the methodology of the attenuation-derived apparent MAE calculation (Section 2.4 of the text), the uncertainty of the apparent MAE estimates could be associated with the measurements and empirical correction parameters used in the equations. To evaluate the potential uncertainties introduced in the calculation, the robustness of the observed relative patterns was evaluated through loading-screening and correction-parameter sensitivity tests, as following:

(i) All samples were selected to recalculate and evaluate the uncertainty caused by the fluctuation of the light attenuation signal in the measurement. The initial values, given directly by the data summary text file, remained the same; and rest values, including the signal at the end of EC_1 stage, at the beginning of EC_2 stage and at the end of EC_3 stage, were replaced by the lowest and highest signal values in the last 5 or 10 seconds to recalculate. Compared to the original results, the mean deviation caused by the signal fluctuation was -2.25%~2.12% for the apparent MAE_{char} and -4.67%~6.45% for the apparent MAE_{soot} (Table S6).

(ii) To evaluate the robustness of the observed relative patterns under different empirical correction parameters, different *C* values were selected based on a ranged reported from 1.3 to 3.5 to recalculate the apparent MAE values using the same other parameters and measurements (Table S7). Despite the maximum deviation up to 42.7% for the apparent MAE of char and soot compared to the current MAE values, the relative patterns that the apparent MAE_{char} values were obviously higher than those of soot and both increased during rainy days compared to non-rainy days did not alter. Similarly, the above method of iterative operation was employed to evaluate the potential uncertainty introduced by *f* value, as showed in Table S8, showing the highest deviations of 25.7% for the apparent MAE_{char} and -14.1% for the apparent MAE_{soot}, but the observed relative differences of the apparent MAE levels between char and soot or between rainy and non-rainy days also did not alter.

(iii) To reduce of the uncertainty caused by the filter-overloading effect, the high-loading samples were censored and eliminated based on the linear fitting equation between the light attenuation and carbon mass per unit area of filter samples. As illustrated in Figure S8, a total of 4 samples were identified as potential filter-overloading samples, representing 3.1% of the total sample set, and these samples were all collected in non-rainy days of the relatively high-pollution winter period. After eliminating these data of the potential filter-overloading samples, the recalculation results of statistical comparisons and correlation analyses did not show any

234 significant changes, indicating that the main conclusions were insensitive to the exclusion of
235 high-loading samples in this study.

236 Table S1 Equations for source apportionment of EC and OC based on LHS method.

Equations	
$POC_{bb} = LG \times (OC/LG)_{bb}$	(S5)
$EC_{bb} = POC_{bb} \times (EC/OC)_{bb} = LG \times (OC/LG)_{bb} \times (EC/OC)_{bb}$	(S6)
$EC_{ff} = EC - EC_{bb}$	(S7)
$OC_{ff} = TC_{ff} - EC_{ff}$	(S8)
$OC_{other,\ nf} = OC_{nf} - POC_{bb}$	(S9)

237

238 Table S2 Central values with low and high limits of input parameters for source
239 apportionment using the LHS method.

Parameters	Low value	Central value	High value
$(LG/OC)_{bb}$	0.07	0.13	0.2
$(EC/OC)_{bb}$	0.03	0.22	0.31
$F_m{}^{14}C_{TC}$	1.005	1.05	1.104

240

Table S3 The mapping of BS-factor to base-factor for the solution of 4 factors (Number of bootstrap runs: 100).

	Factor 1	Factor 2	Factor 3	Factor 4	Unmapped
Boot Factor 1	100	0	0	0	0
Boot Factor 2	0	99	0	0	0
Boot Factor 3	0	0	100	0	0
Boot Factor 4	0	0	0	100	0

Table S4 The DISP diagnostics of the solution of 4 factors.

	Factor 1	Factor 2	Factor 3	Factor 4
Error Code	0			
Largest Decrease in Q	0			
% d_Q	0			
Swaps by Factor	0	0	0	0

Table S5 The distributions of various source contributions to BC, char, and soot based on the ^{14}C-LHS-PMF approach.

Contributions to BC (%)	Mean	Stdev	Minimum	25th percentile	Median	75th percentile	Maximum
Factor 1: Biomass burning	19.6	0.8	17.5	19.4	20.1	20.2	20.2
Factor 2: Coal combustion	21.5	2.2	18.8	18.8	22.8	22.9	24.9
Factor 3: Traffic-related source	31.7	5.4	19.0	31.8	31.9	32.6	47.5
Factor 4: Heavy-oil combustion	27.2	5.2	12.8	25.1	25.2	29.2	38.6
Contributions to char (%)	Mean	Stdev	Minimum	25th percentile	Median	75th percentile	Maximum
Factor 1: Biomass burning	24.1	0.9	21.7	24.0	24.5	24.6	25.5
Factor 2: Coal combustion	19.9	2.3	16.7	17.2	21.6	21.7	21.7
Factor 3: Traffic-related source	26.0	4.6	16.9	25.4	25.4	27.1	41.3
Factor 4: Heavy-oil combustion	30.0	4.6	16.6	28.3	28.4	31.8	39.7
Contributions to soot (%)	Mean	Stdev	Minimum	25th percentile	Median	75th percentile	Maximum
Factor 1: Biomass burning	0.0	0.0	0.0	0.0	0.0	0.0	0.0
Factor 2: Coal combustion	28.4	2.4	27.0	27.1	27.7	27.8	35.1
Factor 3: Traffic-related source	56.5	8.8	39.8	50.9	57.9	64.6	64.6
Factor 4: Heavy-oil combustion	15.1	7.6	7.7	7.7	14.4	22.0	25.1

Table S6 Uncertainty analysis caused by optical attenuation signals in the thermal-optical MAE estimation.

Apparent MAE	Estimation scheme	Mean relative deviation		
		Annual	Non-rainy days	Rainy days
MAE_{Char}	EC_1 end lowest	-2.20%	-2.17%	-2.25%
	EC_2 end highest	2.07%	2.12%	1.97%
MAE_{Soot}	EC_2 begin lowest, EC_3 end lowest	3.52%	4.17%	2.25%
	EC_2 begin highest, EC_3 end highest	-2.24%	-2.41%	-1.90%
	EC_2 begin lowest, EC_3 end highest	5.63%	6.45%	4.01%
	EC_2 begin highest, EC_3 end lowest	-4.33%	-4.67%	-3.65%

Table S7 Uncertainty analysis of apparent MAE_{BC}, MAE_{char}, and MAE_{soot} as a function of different *C* values used in the thermal-optical MAE estimation.

Periods	Parameter *C*	MAE_{BC} ($m^2 \cdot gC^{-1}$)	MAE_{Char} ($m^2 \cdot gC^{-1}$)	MAE_{Soot} ($m^2 \cdot gC^{-1}$)	* *p* value	Uncertainty		
						$Char_{BC}$	$Char_{MAE}$	$Soot_{MAE}$
Annual	1.5	13.52±1.98	10.88±3.90	16.81±6.45	$p < 0.0001$	42.7%	42.7%	42.7%
	2	10.14±1.49	8.16±2.93	12.61±4.84	$p < 0.0001$	7.0%	7.0%	7.0%
	2.14	9.48±1.39	7.63±2.73	11.78±4.52	$p < 0.0001$	0%	0%	0%
	2.5	8.11±1.19	6.53±2.34	10.08±3.87	$p < 0.0001$	14.4%	14.4%	14.4%
	3	6.76±0.99	5.44±1.95	8.40±3.23	$p < 0.0001$	28.7%	28.7%	28.7%
	3.5	5.79±0.85	4.66±1.67	7.20±2.76	$p < 0.0001$	38.9%	38.9%	38.9%
Non-rainy days	1.5	13.37±2.01	11.14±4.16	15.11±6.46	$p < 0.0001$	42.7%	42.7%	42.7%
	2	10.03±1.51	8.36±3.12	11.34±4.85	$p < 0.0001$	7.0%	7.0%	7.0%
	2.14	9.37±1.41	7.81±2.91	10.59±4.53	$p < 0.0001$	0%	0%	0%
	2.5	8.02±1.21	6.68±2.49	9.07±3.88	$p < 0.0001$	14.4%	14.4%	14.4%
	3	6.69±1.01	5.57±2.08	7.56±3.23	$p < 0.0001$	28.7%	28.7%	28.7%
	3.5	5.73±0.86	4.77±1.78	6.48±2.77	$p < 0.0001$	38.9%	38.9%	38.9%
Rainy days	1.5	13.81±1.91	10.37±3.33	20.15±5.00	$p < 0.0001$	42.7%	42.7%	42.7%
	2	10.36±1.43	7.78±2.49	15.12±3.75	$p < 0.0001$	7.0%	7.0%	7.0%
	2.14	9.68±1.34	7.27±2.33	14.13±3.50	$p < 0.0001$	0%	0%	0%
	2.5	8.29±1.14	6.22±2.00	12.09±3.00	$p < 0.0001$	14.4%	14.4%	14.4%
	3	6.91±0.95	5.19±1.66	10.08±2.50	$p < 0.0001$	28.7%	28.7%	28.7%
	3.5	5.92±0.82	4.45±1.43	8.64±2.14	$p < 0.0001$	38.9%	38.9%	38.9%

* *p*-value indicates a statistically significant difference between MAE_{char} and MAE_{soot}.

Table S8 Uncertainty analysis of MAE_{BC}, MAE_{char}, and MAE_{soot} as a function of different *f* values used in the thermal-optical MAE estimation.

Periods	Parameter *f*	MAE_{BC} ($m^2 \cdot gC^{-1}$)	MAE_{Char} ($m^2 \cdot gC^{-1}$)	MAE_{Soot} ($m^2 \cdot gC^{-1}$)	* *p* value	Uncertainty		
						MAE_{BC}	$Char_{MAE}$	$Soot_{MAE}$
Annual	0.9	7.06±1.10	5.91±1.86	10.22±3.33	$p < 0.0001$	-25.5%	-20.0%	-10.3%
	1	8.21±1.23	6.74±2.26	11.01±3.92	$p < 0.0001$	-13.4%	-10.4%	-5.1%
	1.05	8.83±1.30	7.17±2.49	11.40±4.22	$p < 0.0001$	-6.9%	-5.3%	-2.6%
	1.1	9.48±1.39	7.63±2.73	11.78±4.52	$p < 0.0001$	0%	0%	0%
	1.15	10.16±1.49	8.11±3.01	12.16±4.83	$p < 0.0001$	7.3%	5.5%	2.5%
	1.2	10.89±1.61	8.61±3.31	12.54±5.14	$p < 0.0001$	14.9%	11.3%	5.1%
	1.3	12.49±1.93	9.70±4.00	13.30±5.78	$p < 0.0001$	31.8%	23.8%	10.1%
Non-rainy days	0.9	6.93±1.06	5.96±1.95	9.32±3.29	$p < 0.0001$	-26.0%	-21.0%	-8.3%
	1	8.09±1.22	6.84±2.39	9.96±3.90	$p < 0.0001$	-13.7%	-11.0%	-4.2%
	1.05	8.71±1.31	7.31±2.64	10.28±4.21	$p < 0.0001$	-7.0%	-5.6%	-2.1%
	1.1	9.37±1.41	7.81±2.91	10.59±4.53	$p < 0.0001$	0%	0%	0%
	1.15	10.07±1.53	8.33±3.21	10.91±4.86	$p < 0.0001$	7.5%	5.9%	2.1%
	1.2	10.82±1.68	8.89±3.54	11.23±5.19	$p < 0.0001$	15.4%	12.1%	4.2%
	1.3	12.47±2.06	10.11±4.31	11.86±5.86	$p < 0.0001$	33.0%	25.7%	8.4%
Rainy days	0.9	7.32±1.13	5.81±1.68	12.01±2.63	$p < 0.0001$	-24.5%	-18.1%	-14.1%
	1	8.45±1.23	6.53±1.98	13.08±3.06	$p < 0.0001$	-12.8%	-9.2%	-7.0%
	1.05	9.05±1.28	6.89±2.15	13.61±3.28	$p < 0.0001$	-6.5%	-4.7%	-3.5%
	1.1	9.68±1.34	7.27±2.33	14.13±3.50	$p < 0.0001$	0%	0%	0%
	1.15	10.34±1.40	7.66±2.52	14.64±3.74	$p < 0.0001$	6.8%	4.8%	3.4%
	1.2	11.03±1.47	8.05±2.73	15.14±3.97	$p < 0.0001$	14.0%	9.7%	6.8%
	1.3	12.51±1.65	8.88±3.19	16.14±4.46	$p < 0.0001$	29.4%	20.0%	13.3%

* *p*-value indicates a statistically significant difference between MAE_{char} and MAE_{soot}.

Table S9 Mean values of mass concentrations, attenuation-derived apparent light absorptions (Abs), apparent MAE, and associated ratios of carbonaceous components in $PM_{2.5}$ for the campaign over Lin'an.

	Winter	**Spring**	**Summer**	**Autumn**	**Annual**
TC ($\mu gC \cdot m^{-3}$)	8.71±4.45 (2.89~18.06)	8.67±2.73 (4.99~15.36)	5.82±2.29 (1.96~10.6)	8.81±2.52 (5.38~17.1)	7.88±3.26 (1.96~18.06)
OC ($\mu gC \cdot m^{-3}$)	5.52±2.95 (1.67~11.38)	6.16±2.22 (3.14~11.72)	4.16±1.83 (1.17~8.14)	6.17±1.81 (3.58~11.96)	5.44±2.33 (1.17~11.96)
BC ($\mu gC \cdot m^{-3}$)	3.19±1.59 (1.1~6.68)	2.51±0.71 (1.25~4.52)	1.66±0.51 (0.79~2.57)	2.64±0.88 (1.57~5.14)	2.44±1.1 (0.79~6.68)
Char ($\mu gC \cdot m^{-3}$)	2.82±1.61 (0.78~6.35)	1.96±0.73 (0.89~4.05)	1.07±0.39 (0.44~1.75)	2.35±0.91 (1.35~4.91)	1.98±1.16 (0.44~6.35)
Soot ($\mu gC \cdot m^{-3}$)	0.37±0.12 (0.18~0.71)	0.54±0.15 (0.28~0.85)	0.6±0.18 (0.29~0.99)	0.29±0.13 (0.13~0.64)	0.46±0.2 (0.13~0.99)
BC/TC (%)	37.47±4.13 (27.69~43.78)	29.82±6.09 (20.13~41.22)	29.72±4.86 (23.09~40.97)	30.02±4.92 (21.91~41.4)	31.44±5.88 (20.13~43.78)
Char/BC (%)	85.18±8.55 (61.54~96.82)	76.92±8.17 (59.86~90.77)	63.16±8.05 (46.75~79.96)	87.88±6.6 (68~96.6)	77.49±12.73 (46.75~96.82)
Soot/BC (%)	14.82±8.55 (3.18~38.46)	23.08±8.17 (9.23~40.14)	36.84±8.05 (20.04~53.25)	12.12±6.6 (3.4~32)	22.51±12.73 (3.18~53.25)
OC/BC	1.7±0.32 (1.28~2.61)	2.49±0.71 (1.43~3.97)	2.45±0.54 (1.44~3.33)	2.41±0.54 (1.42~3.56)	2.29±0.62 (1.28~3.97)
Char/Soot	8.64±6.65 (1.6~30.43)	3.99±2.1 (1.49~9.84)	1.86±0.7 (0.88~3.99)	9.86±6.17 (2.13~28.41)	5.88±5.6 (0.88~30.43)
MAE_{BC} ($m^2 \cdot gC^{-1}$)	9±1.18 (6.87~11.08)	8.89±1.04 (6.87~11.9)	9.44±1.49 (7.25~14.85)	10.44±1.21 (8.16~13.56)	9.48±1.39 (6.87~14.85)
MAE_{char} ($m^2 \cdot gC^{-1}$)	8.23±1.35 (5.06~10.99)	7.1±1.85 (2.54~9.99)	5.44±2.68 (0.83~11.9)	10.11±1.98 (4.48~13.85)	7.64±2.73 (0.83~13.85)
MAE_{soot} ($m^2 \cdot gC^{-1}$)	10.06±4.97 (1.54~21.16)	12.72±3.56 (5.76~19.58)	14.96±2.42 (10.7~22.07)	8.77±4.16 (2.67~19.42)	11.78±4.5 (1.54~22.07)
Abs_{BC} ($M \cdot m^{-1}$)	27.36±10.77 (10.19~49.8)	22.13±6.3 (13.07~40.85)	15.32±4.19 (8.19~23.44)	27.05±7.32 (15.67~47.11)	22.52±8.79 (8.19~49.8)
Abs_{char} ($M \cdot m^{-1}$)	22.89±12.38 (5.54~49.22)	14.3±7.34 (3.74~33.1)	5.83±3.46 (0.36~12.94)	23.64±9.09 (6.05~46.35)	16.06±11.18 (0.36~49.22)
Abs_{soot} ($M \cdot m^{-1}$)	3.89±2.47 (0.46~9.2)	7.05±2.83 (1.73~12.01)	8.92±3.15 (3.86~15.88)	2.93±2.98 (0.61~11.72)	5.85±3.8 (0.46~15.88)

Table S10 Comparison of BC, char, and soot concentrations in $PM_{2.5}$ measured in this study with those reported previously (Unit: μgC·m^{-3})

Location	Sampling time	Region	Station type	BC	Char	Soot	Reference
Lin'an	Dec. 2019 to Nov. 2020 (Annual)	YRD Region	Regional Background Site	2.44±1.10	2.82±1.61	0.37±0.12	This study
	Winter			3.19±1.59	1.96±0.73	0.54±0.15	
	Spring			2.51±0.71	1.07±0.39	0.6±0.18	
	Summer			1.66±0.51	2.35±0.91	0.29±0.13	
	Autumn			2.64±0.88	1.98±1.16	0.46±0.2	
Lin'an	Jun. 2015 to May 2016 (Annual)	YRD Region	Regional Background Site	4.30±2.11	-	-	(Liang et al., 2020)
	Spring			3.99±1.99	-	-	
	Summer			3.38±1.49	-	-	
	Autumn			5.16±1.77	-	-	
	Winter			4.63±2.59	-	-	
Lin'an	Aug. 2014 to Sept. 2015 (Annual)	YRD Region	Regional Background Site	3.88±1.70	-	-	(Chen, 2018)
	Spring			4.63±1.45	-	-	
	Summer			2.42±1.00	-	-	
	Autumn			4.49±1.57	-	-	
	Winter			4.40±1.64	-	-	
Mt. Wuyi	Mar. 2014 to Feb. 2015 (Annual)	Southeast China	Alpine Background Site	0.56±0.09	-	-	(Ren et al., 2019)
	Spring			0.51±0.11	-	-	
	Summer			0.48±0.20	-	-	
	Autumn			0.56±0.15	-	-	
	Winter			0.69±0.13	-	-	
Beihuangcheng Island	Aug. 2014 to Sept. 2015 (Annual)	North China	Coastal Background Site	2.28±1.69	-	-	(Zong et al., 2018)
	Spring			2.24±1.27	-	-	
	Summer			1.60±0.89	-	-	
	Autumn			2.34±1.20	-	-	
	Winter			2.86±2.67	-	-	
Chongming Island	Dec. 2018 to Dec. 2019 (Annual)	YRD Region	Coastal Background Site	2.1±1.6	-	-	(Xing, 2022)
Xieyang Island	May 2015 to May 2016 (Annual)	South China	Coastal Background Site	1.64±1.00	1.51±1.01	0.13±0.08	(Geng et al., 2024)
Lijiang	Mar. to May 2018 (Spring)	Southwest China	High-Altitude Remote Site	0.68±0.36	0.56±0.33	0.12±0.07	(Zhao et al., 2015)
Shanghai	Jul. 2009 (Summer)	YRD Region	Urban Site	3.68±1.27	3.00±1.24	0.68±0.30	(Huang et al., 2014)
	Jan. 2019 (Winter)			5.53±2.36	5.11±2.35	0.42±0.17	

Changzhou	Jul. to Aug. 2016 (Summer) Oct. to Nov. 2016 (Autumn)	YRD Region	Urban Site	3.3±1.2 3.5±1.8	- -	- -	(Ye et al., 2017)
Nanjing Suzhou	Jan. 2015 (Winter)	YRD Region	Urban Site	5.39±3.07 6.40±4.29	- -	- -	(Kang et al., 2018)

263

Table S11 Statistical test results of multiple linear regression calculation for apparent MAE in all days.

All days	Coefficients	T-value	*p*-value	95% Confidence Interval			R^2
				Lower Limit	Upper Limit	Half-Width	
BC_{bb}	7.82±0.46	17.15	*p*<0.0001	6.92	8.72	0.90	0.98
BC_{ff}	9.38±0.21	45.59		8.97	9.78	0.41	
$Char_{bb}$	8.08±0.60	15.11	*p*<0.0001	7.89	10.26	1.19	0.947
$Char_{ff}$	7.41±0.34	23.21		7.23	8.58	0.67	
$Soot_{bb}$	-	-	*p*<0.0001	-	-	-	0.928
$Soot_{ff}$	13.54±0.33	40.66		12.88	14.20	0.66	

Table S12 Statistical test results of multiple linear regression calculation for apparent MAE in non-rainy days.

Non-rainy days	Coefficients	T-value	*p*-value	95% Confidence Interval			R^2
				Lower Limit	Upper Limit	Half-Width	
BC_{bb}	7.84±0.56	14.11	*p*<0.0001	6.73	8.94	1.10	0.98
BC_{ff}	9.29±0.28	33.20		8.74	9.85	0.56	
$Char_{bb}$	8.79±0.72	12.28	*p*<0.0001	7.37	10.22	1.42	0.95
$Char_{ff}$	8.23±0.44	18.53		7.35	9.11	0.88	
$Soot_{bb}$	-	-	*p*<0.0001	-	-	-	0.91
$Soot_{ff}$	13.10±0.43	30.13		12.22	13.94	0.86	

Table S13 Statistical test results of multiple linear regression calculation for apparent MAE in rainy days.

Rainy days	Coefficients	T-value	*p*-value	95% Confidence Interval			R^2
				Lower Limit	Upper Limit	Half-Width	
BC_{bb}	8.55±1.01	8.45	*p*<0.0001	6.51	10.60	2.05	0.99
BC_{ff}	9.44±0.27	35.33		8.90	9.98	0.54	
$Char_{bb}$	10.60±1.4	7.53	*p*<0.0001	7.73	13.40	2.83	0.96
$Char_{ff}$	6.87±0.50	13.85		5.87	7.87	1.00	
$Soot_{bb}$	-	-	*p*<0.0001	-	-	-	0.96
$Soot_{ff}$	14.5±0.47	30.79		13.51	15.40	0.95	

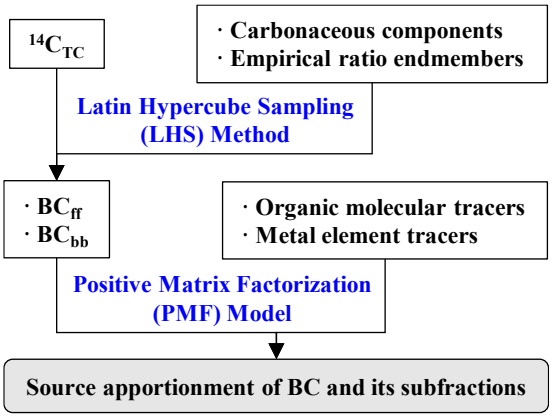


Figure S1 Technique flowchart of source apportionment based on ^{14}C-LHS-PMF method.

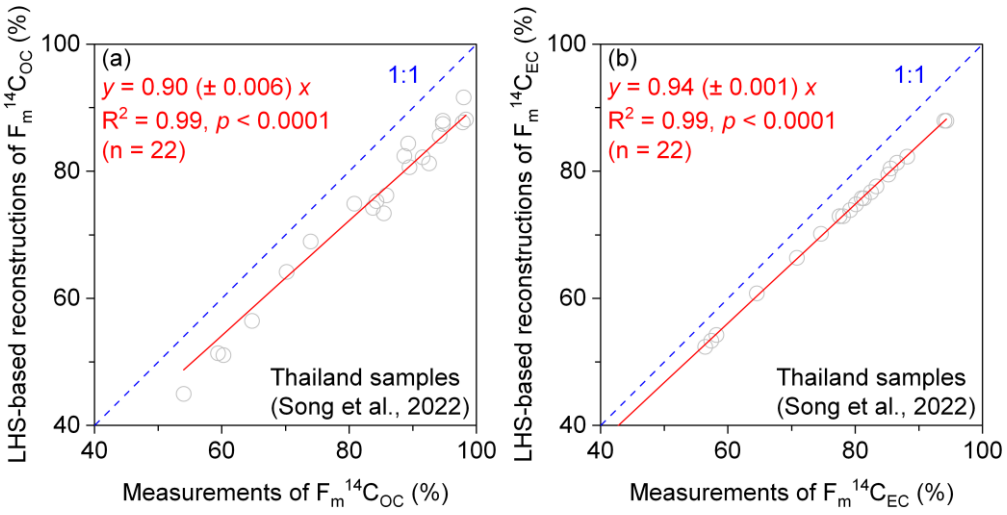


Figure S2 Comparison between $F_m{}^{14}C_{EC}$ measurements by AMS and ^{14}C-constraint LHS-based reconstructed values for $PM_{2.5}$ samples collected in Thailand in our previous study (Song et al., 2022).

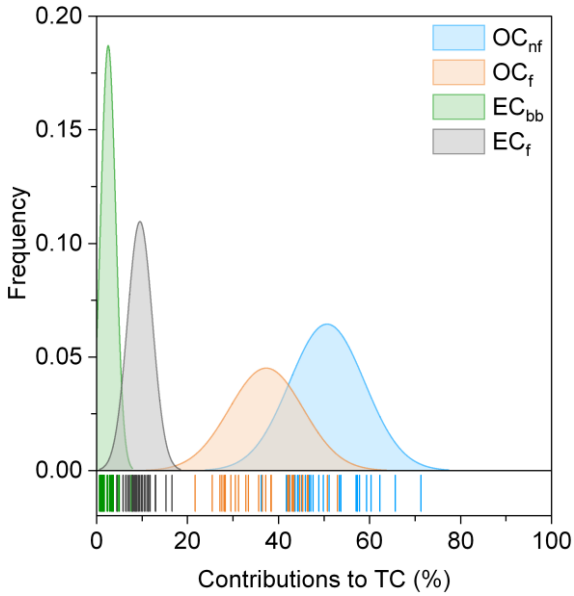
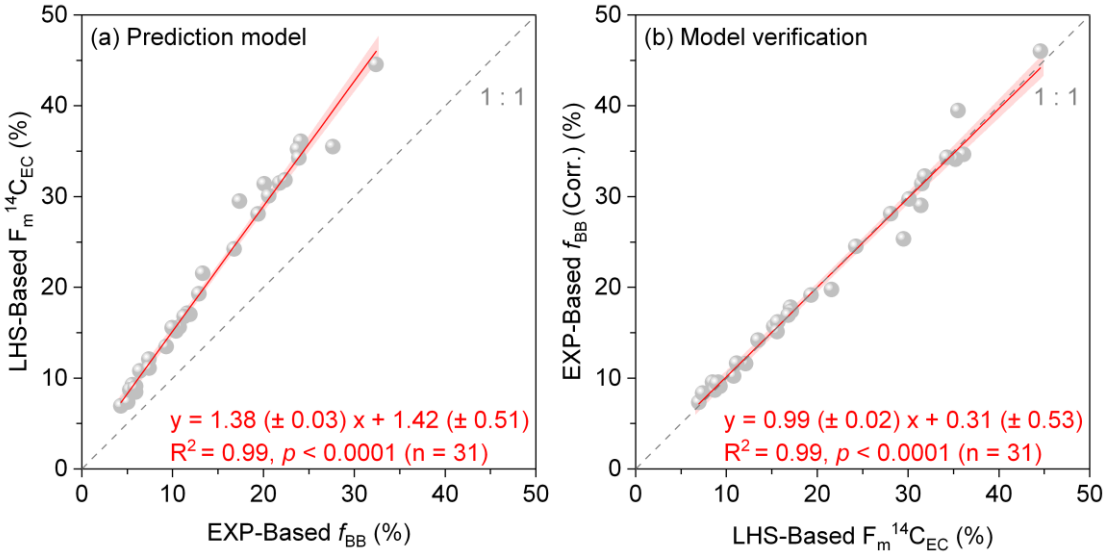


Figure S3 Frequency distributions of the contributions to TC from OC and EC source categories for samples collected at Lin'an based on ^{14}C-constraint LHS method.



282

283 Figure S4 Modern carbon fractions of BC fitted and estimated based on few-shot ^{14}C-

284 measurement and characteristic endmembers.

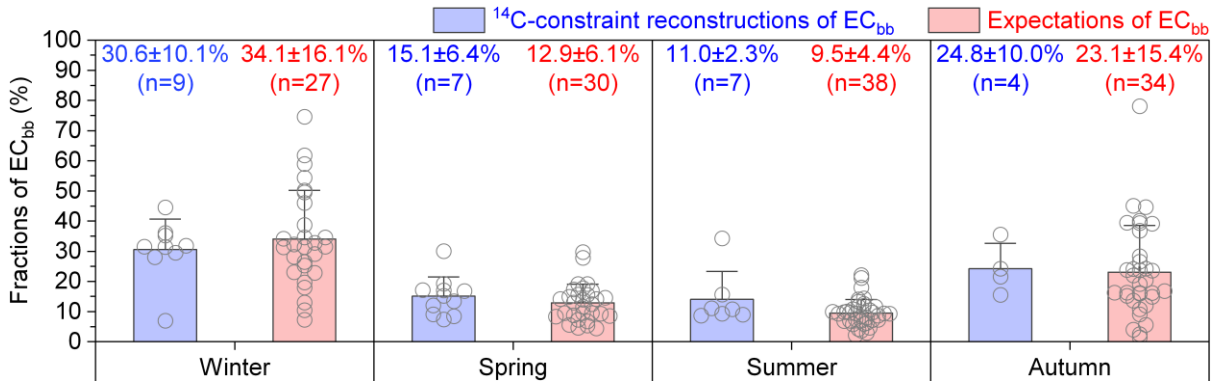


Figure S5 Comparisons between the ^{14}C-constraint LHS-based reconstructed values and expectations of EC_{bb} corrected by the linear equation from the Figure S3.

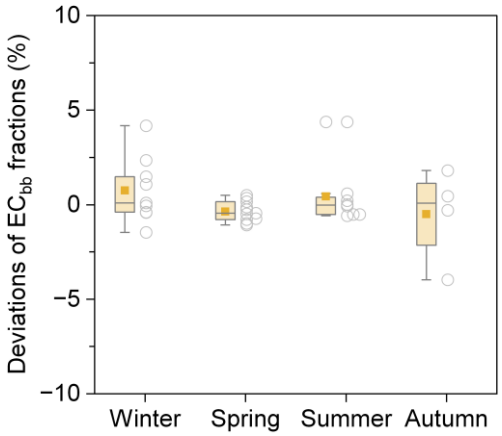
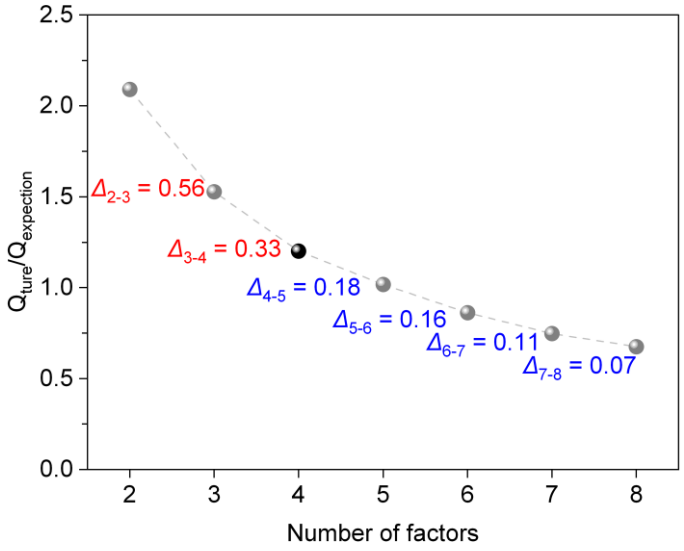


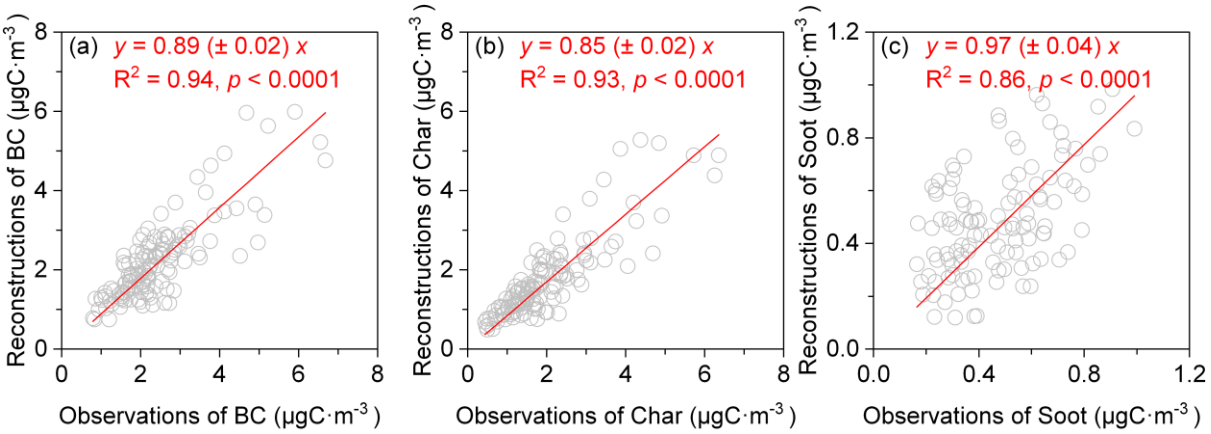
Figure S6 Deviations of the EC_{bb} expectations corrected by the linear equation compared to ^{14}C-constraint LHS-based reconstructions.



291

292 Figure S7 Variation characteristics of $Q_{true}/Q_{expection}$ with the number of factors in PMF model.

293 ($\Delta_{m\text{-}n}$ is the decrease in $Q_{true}/Q_{expection}$ when the number of factors increased from *m* to *n*.)



294

295 Figure S8 Scatter distributions and curves of linear regression equation between the
296 predictions and observations of (a) BC, (b) char, and (c) soot concentrations in the ^{14}C-LHS-
297 PMF simulation.

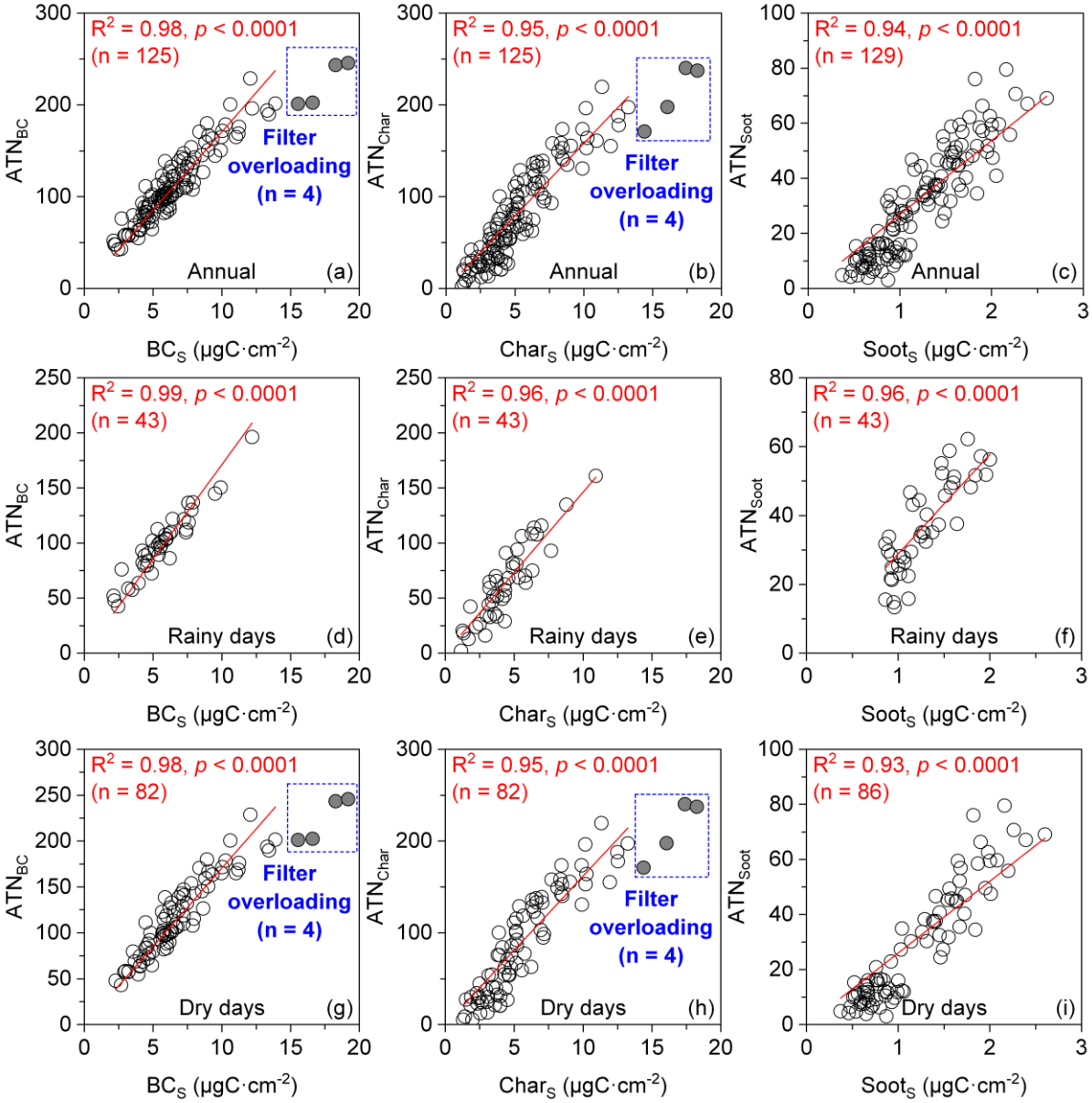
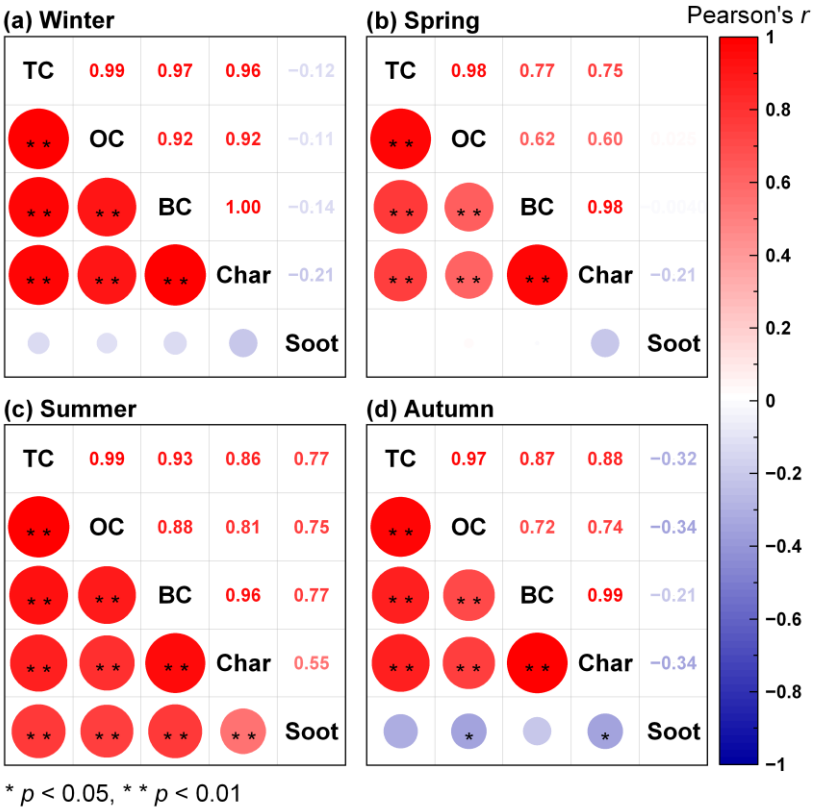


Figure S9 The distribution of the ATN level with BC, char, and soot contents per unit area on the filter.



301

302 Figure S10 Seasonal correlation matrix among various carbonaceous component in $PM_{2.5}$ at
303 Lin'an during the sampling period. Colored and scaled by *r*: the deeper color and larger size
304 represent the higher *r*.

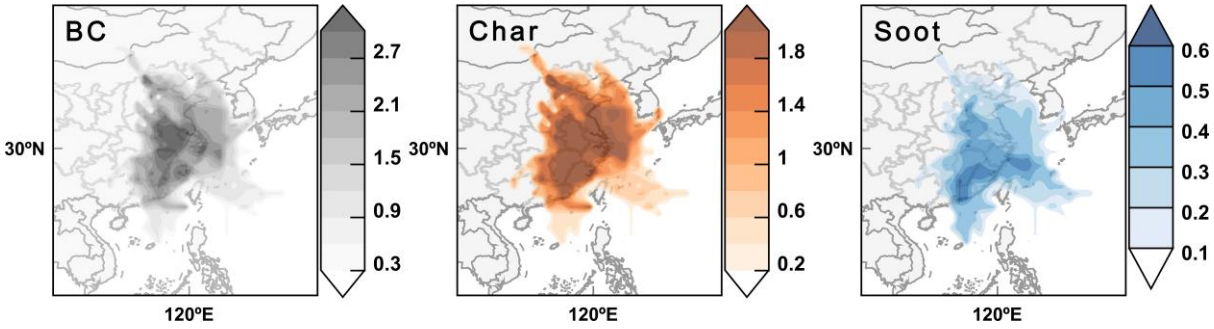


Figure S11 The mass concentration weighted trajectory (CWT) analysis of Char (colored green) and Soot (colored orange) based on NOAA HYSPLIT model for the year-round collections over Lin'an during December 2019 to November 2020.

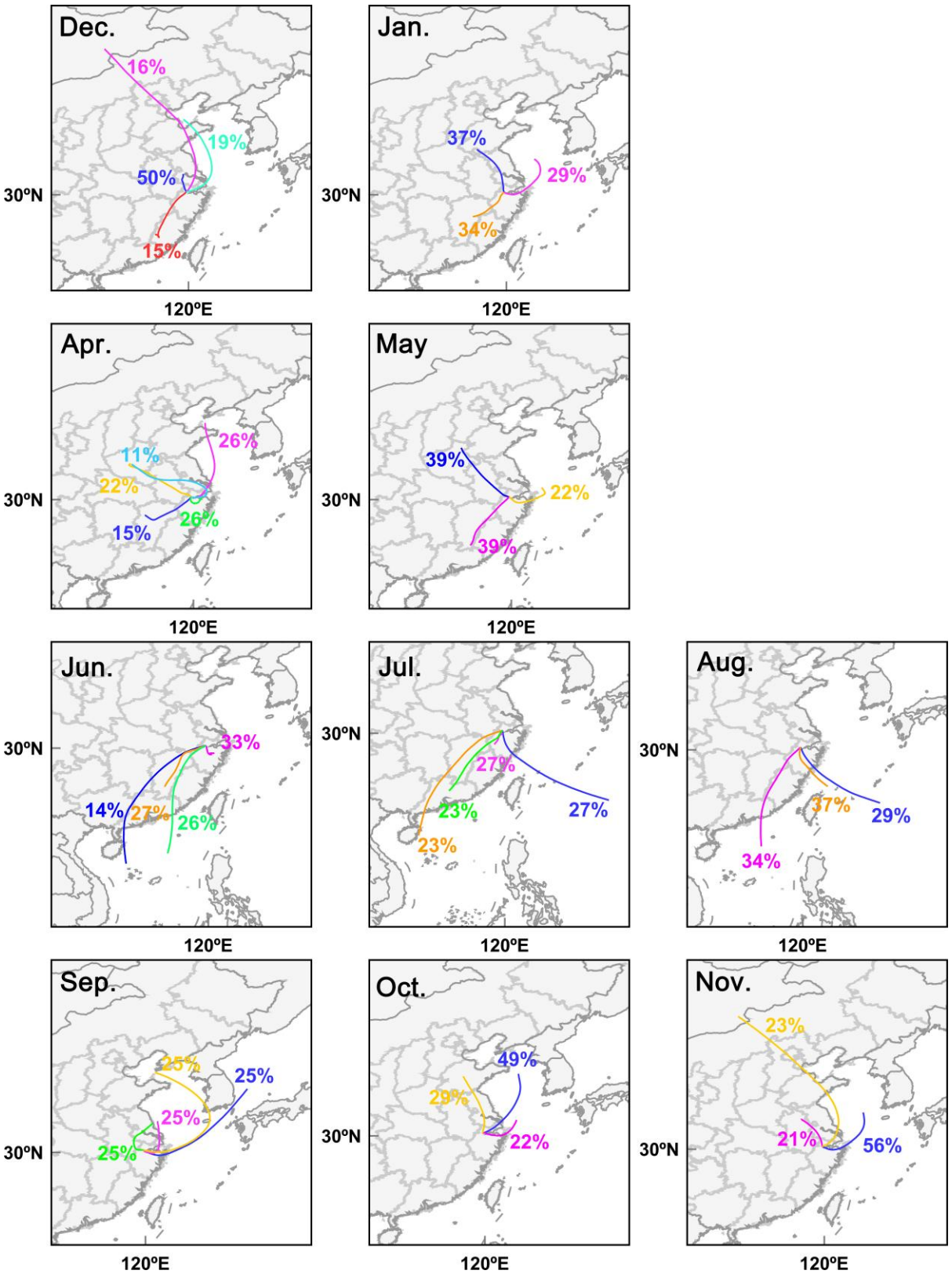
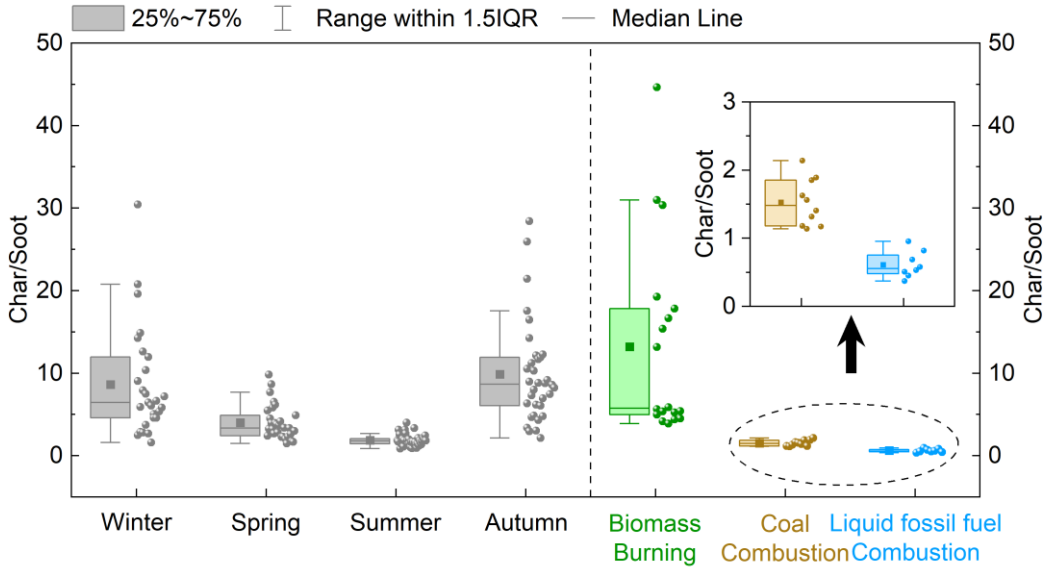
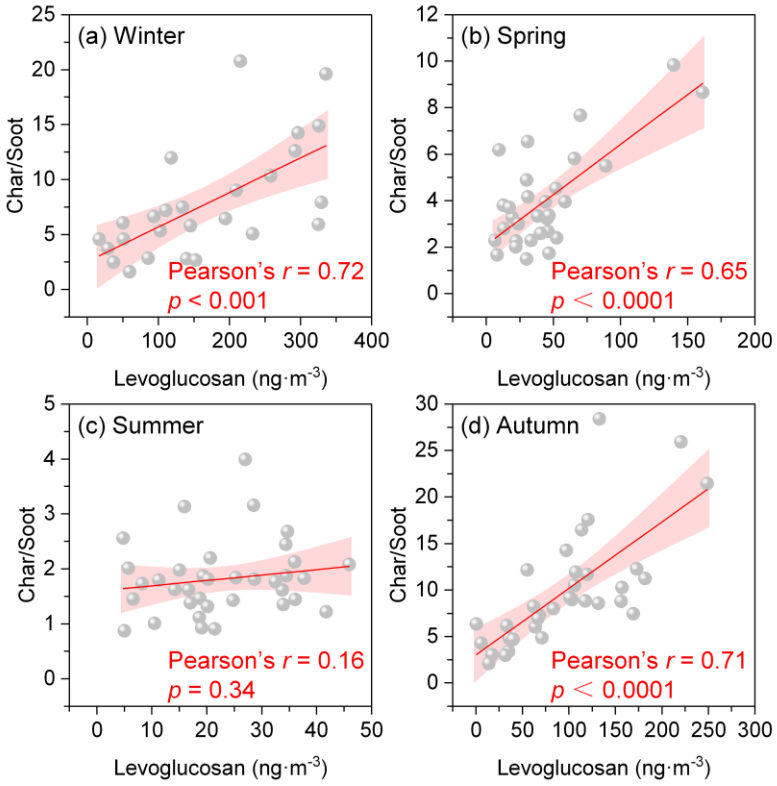


Figure S12 48-h mean backward trajectory path (500m) of monthly identified clusters along based on NOAA HYSPLIT model for the year-round collections over Lin'an during December 2019 to November 2020.



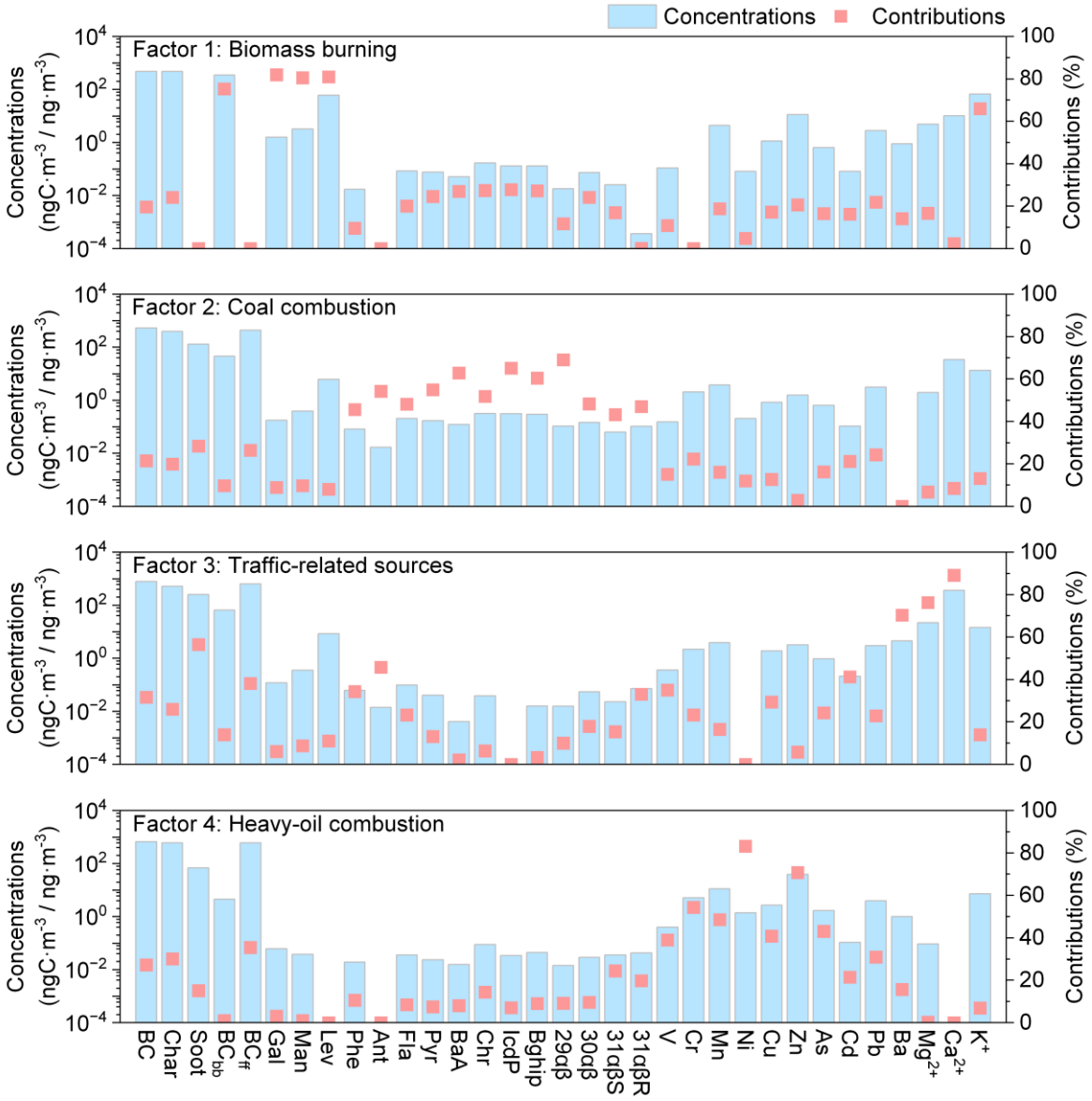
313

314 Figure S13 Seasonal distribution of char/soot ratios measured in this study and the diagnostic
315 ratios ranges of the type of combustion materials obtained from literature research (Cao et al.,
316 2007; Chen et al., 2007; Chow et al., 2004).



317

318 Figure S14 Seasonal scatter distributions and curves of linear regression equation between
319 char/soot ratios and levoglucosan concentrations in $PM_{2.5}$ at Lin'an during the sampling
320 period. (Confidence intervals were shaded in pink.)



321

322 Figure S15 Source profiles (bars) of four factors and the percentage (dots) of species for each
323 factor resolved by PMF model where BC was set as the total variable.

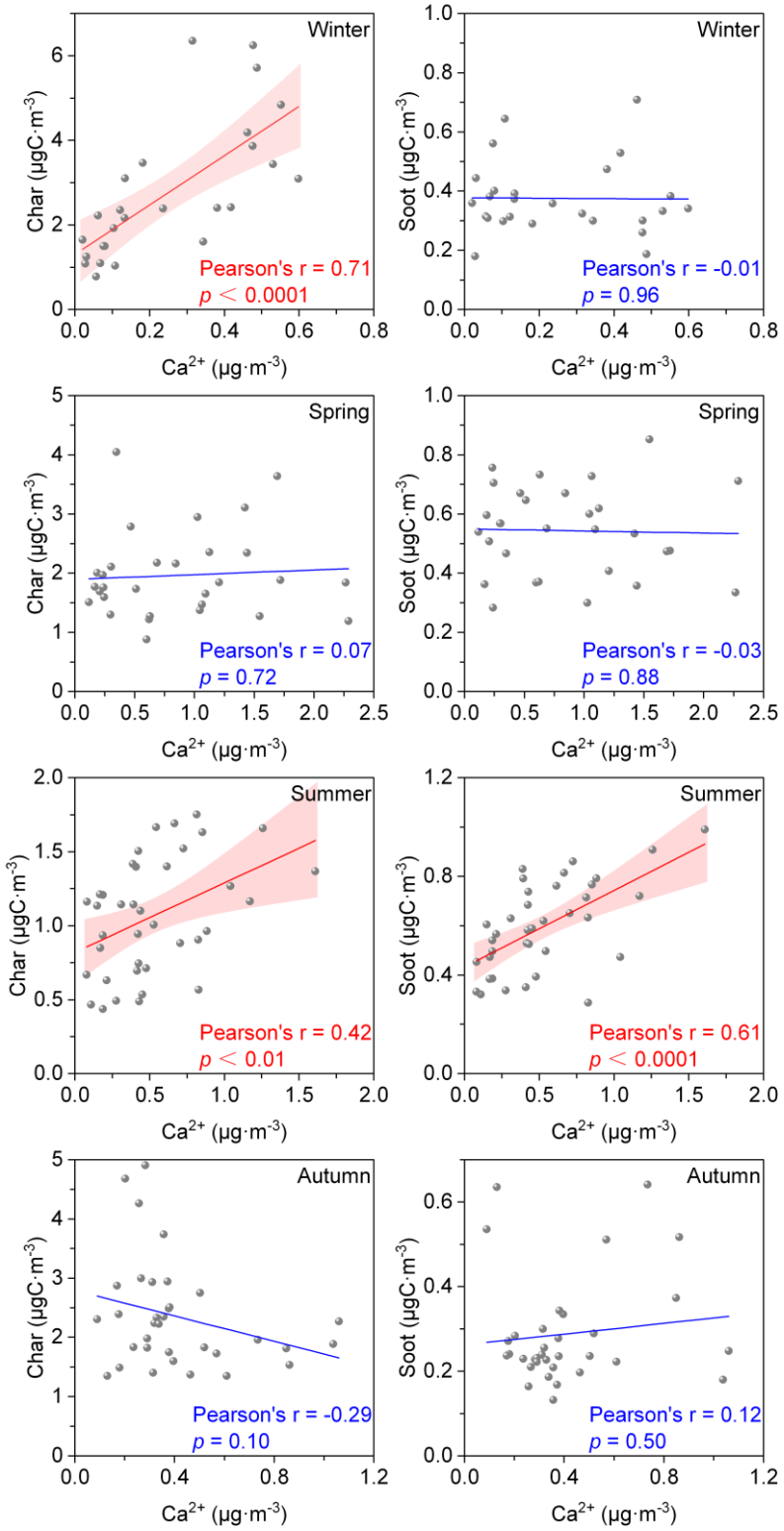


Figure S16 Seasonal scatter distributions and curves of linear regression equation between char, soot with Ca^{2+} concentrations in $PM_{2.5}$ at Lin'an during the sampling period. (Significant items ($p < 0.05$) showed confidence intervals, and confidence intervals were shaded in pink.)

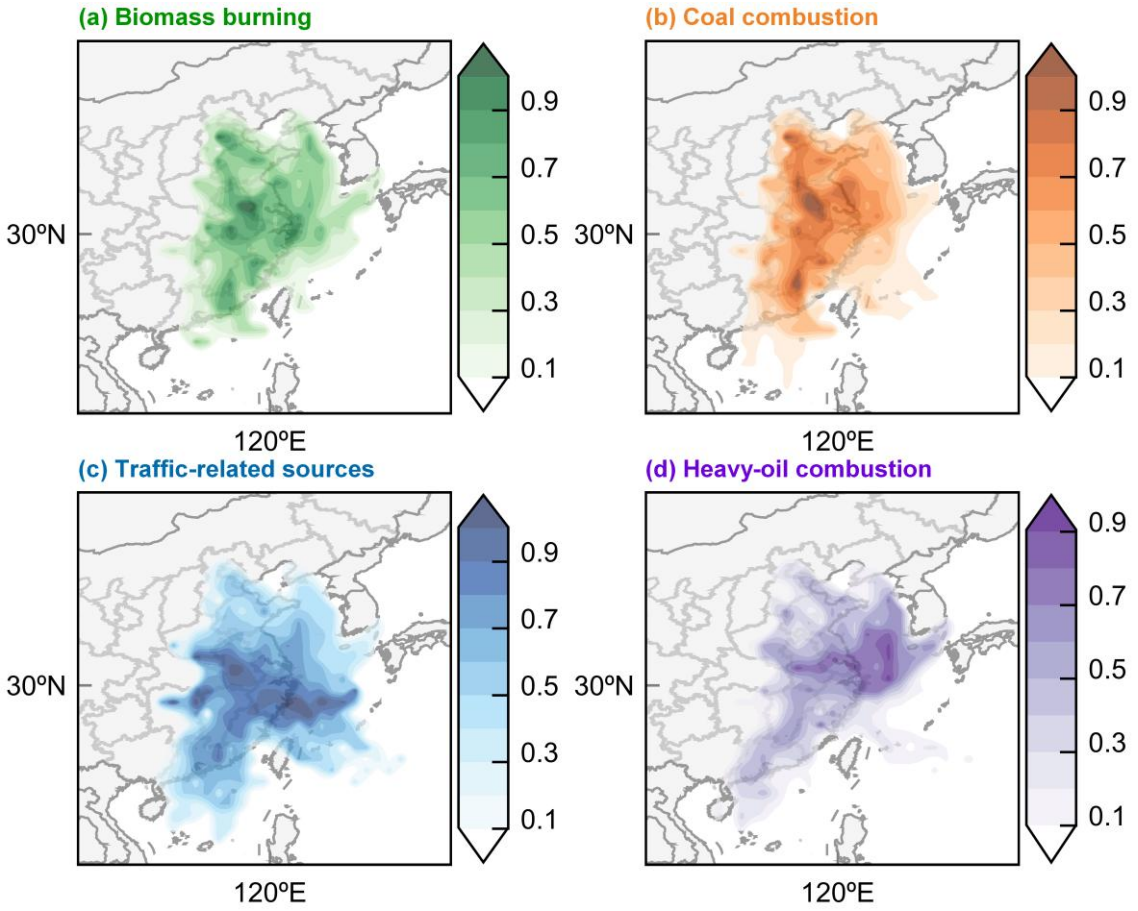


Figure S17 The mass concentration weighted trajectory analysis of BC from various sources based on NOAA HYSPLIT model and PMF model for the year-round collections over Lin'an during December 2019 to November 2020.

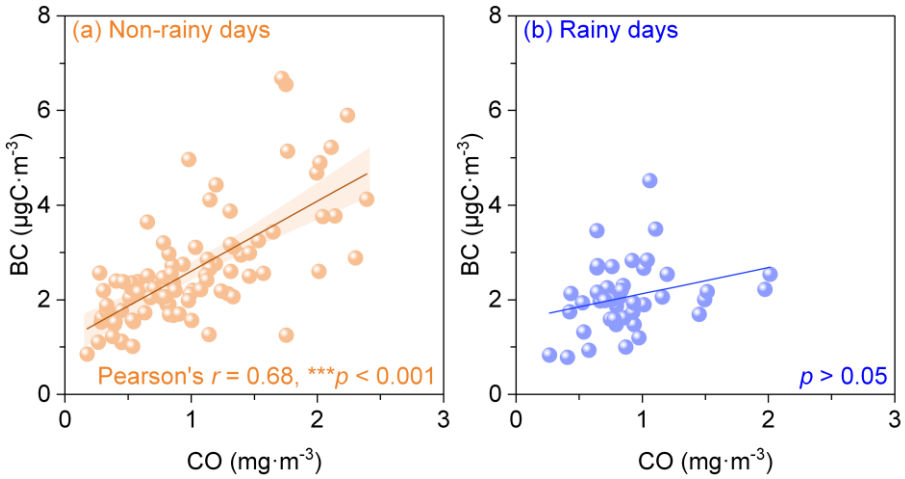


Figure S18 Scatter distributions and curves of linear regression equation between BC in $PM_{2.5}$ with CO concentrations on non-rainy days (a) and rainy days (b) at Lin'an. (Significant items ($p < 0.05$) showed confidence intervals, and confidence intervals were shaded in shadow color.)

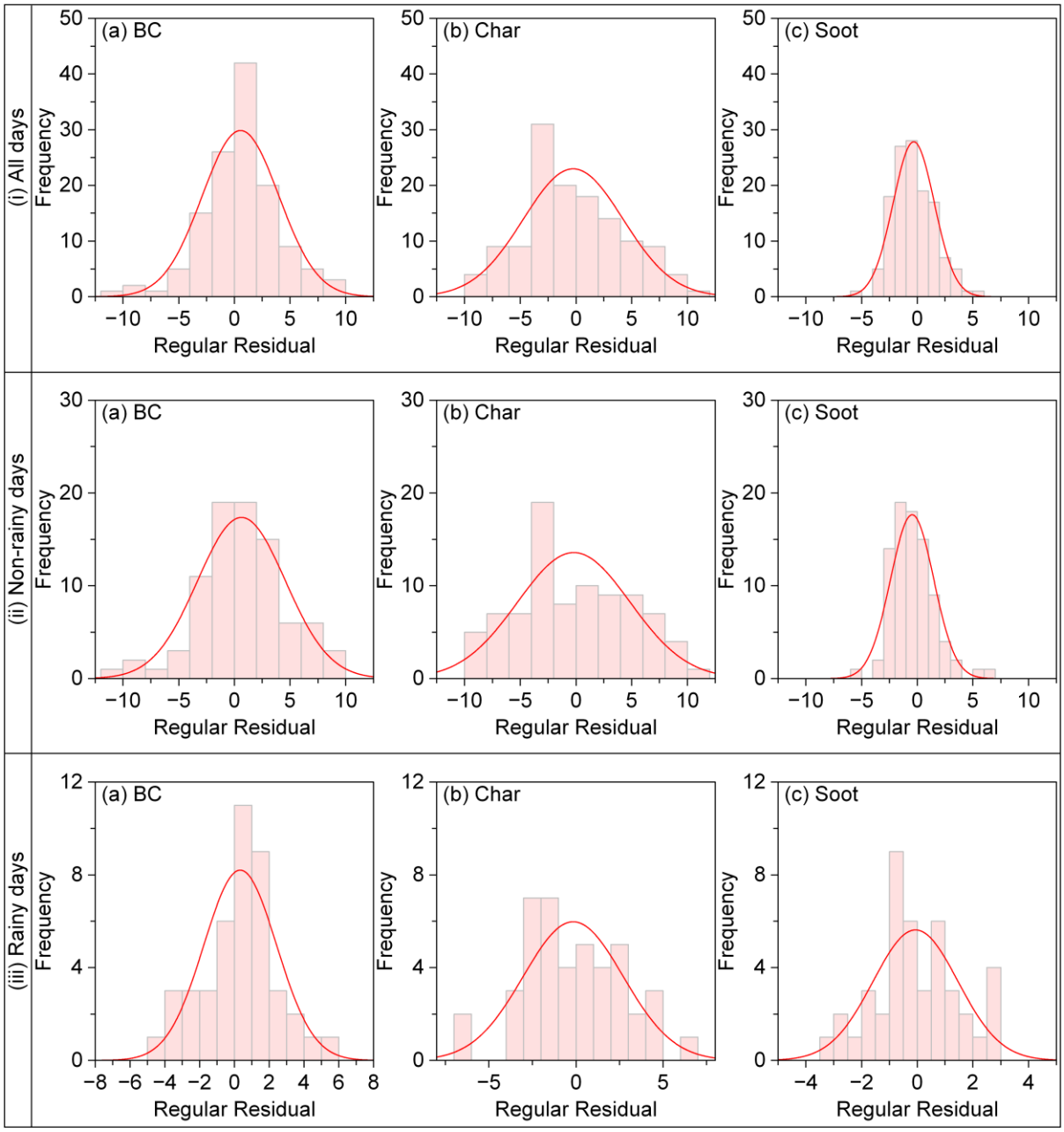
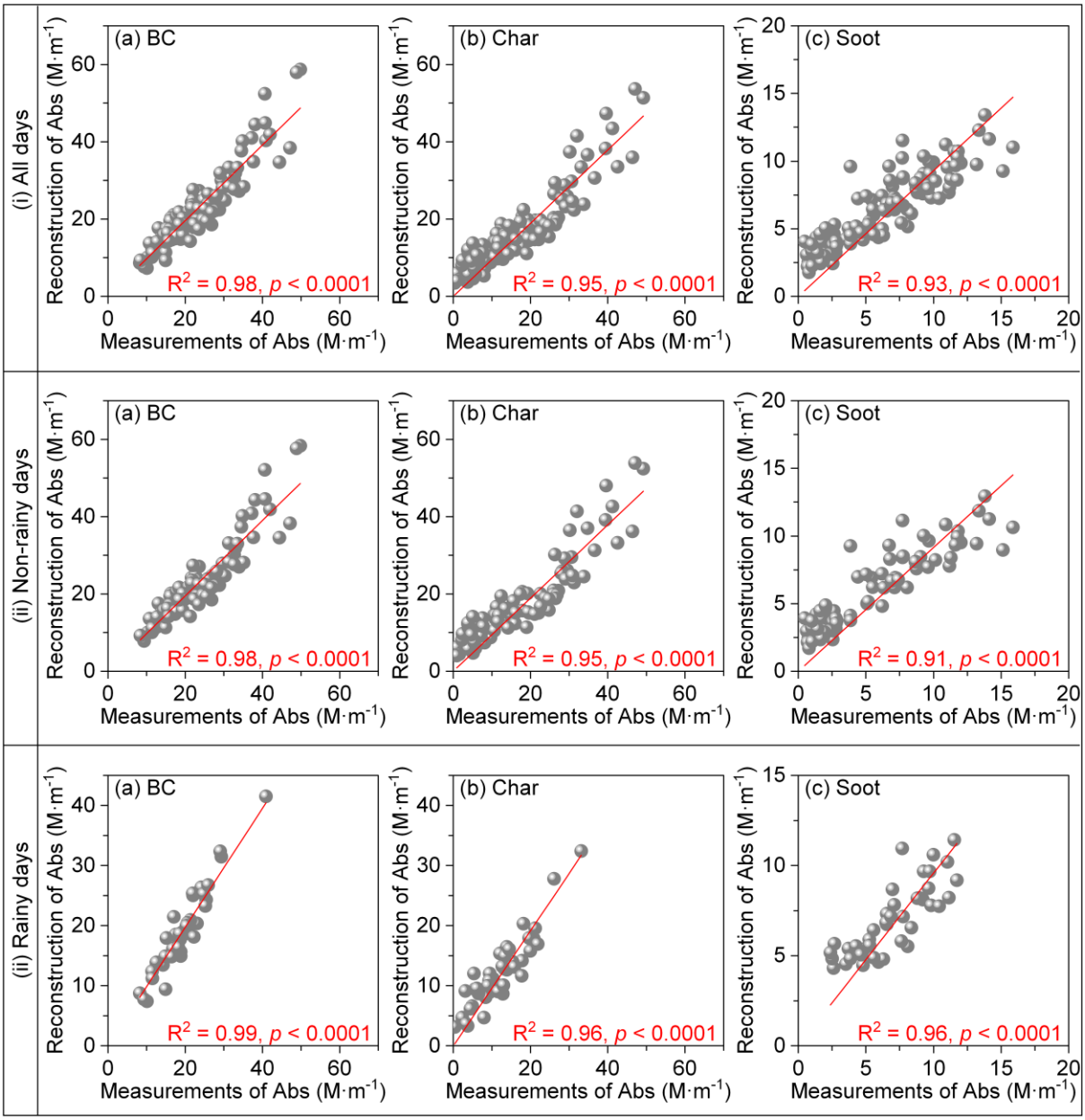


Figure S19 Random distribution of residuals of multiple linear regression fitting equations.



341

342 Figure S20 Scatter distribution of Abs (i.e., MAE_{BC}·BC, MAE_{Char}·Char, and MAE_{Soot}·Soot)
343 from simulations and measurements.

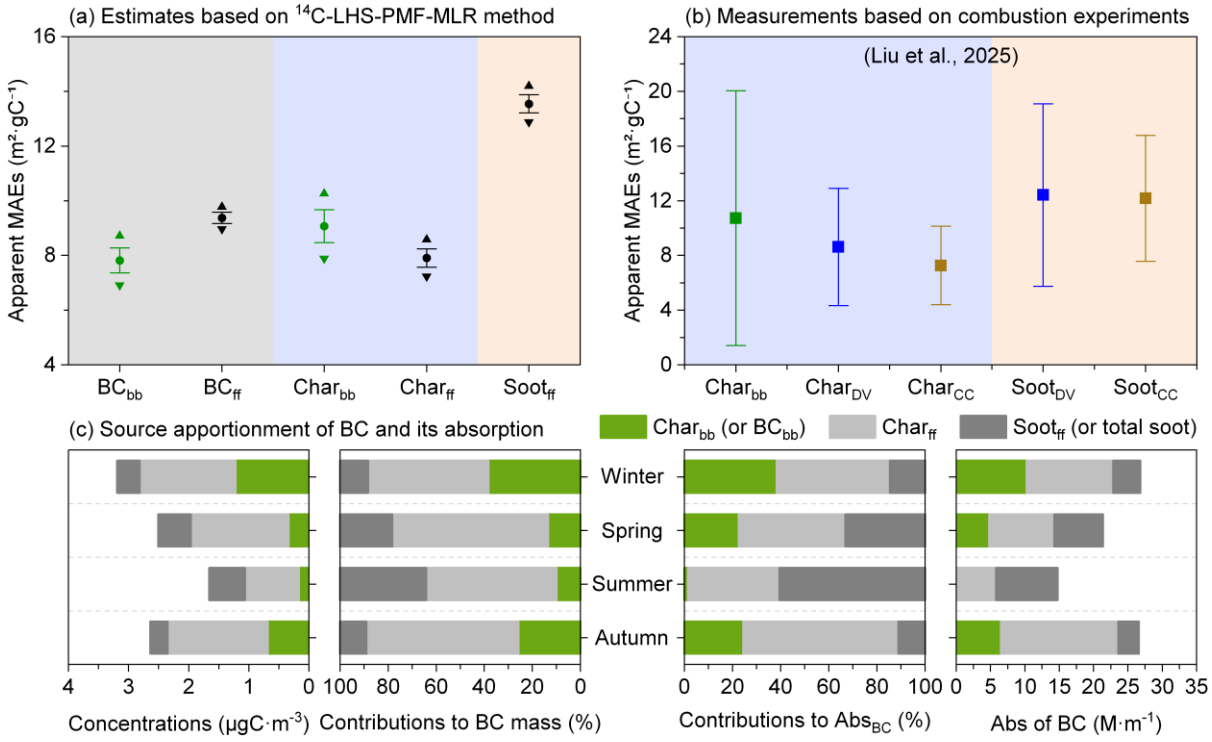


Figure S21 (a) The apparent MAE_{BC}, MAE_{char}, and MAE_{soot} of various sources based on multiple linear regression calculation. The triangles are the upper and lower limits of the 95% confidence interval, and the dots are the means and standards deviation of the simulation. (b) The apparent MAE_{char}, and MAE_{soot} measurements of various sources based on combustion experiment from the literature (Liu et al., 2025). (c) Seasonal patterns of atmospheric mass concentrations, apparent light absorption and their contribution fractions for BC and its subfractions from BB and fossil-fuel-related sources based on ^{14}C-LHS-PMF-MLR model.

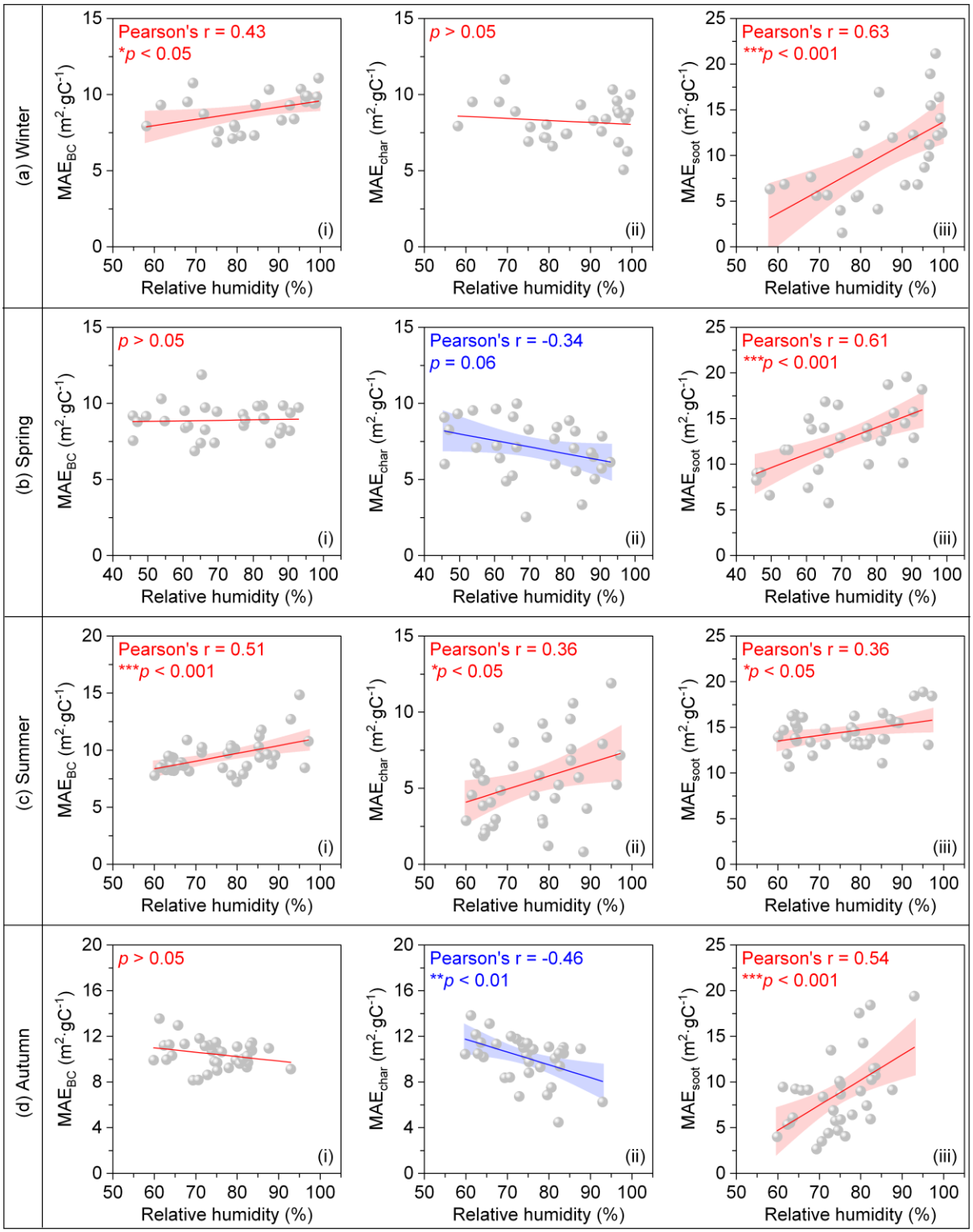


Figure S22 Seasonal scatter distributions and curves of linear regression equation between the apparent MAE of BC, char, and soot with air relative humidity at Lin'an during the sampling period. (Significant items ($p < 0.05$) showed confidence intervals, and confidence intervals were shaded in shadow color.)

REFERENCE

Brown, S. G., Eberly, S., Paatero, P., and Norris, G. A.: Methods for estimating uncertainty in PMF solutions: Examples with ambient air and water quality data and guidance on reporting PMF results, Science of The Total Environment, 518-519, 626-635, https://doi.org/10.1016/j.scitotenv.2015.01.022, 2015.

Cao, F., Zhang, Y.-X., Lin, X., and Zhang, Y.-L.: Characteristics and source apportionment of non-polar organic compounds in $PM_{2.5}$ from the three megacities in Yangtze River Delta region, China, Atmospheric Research, 252, 105443, https://doi.org/10.1016/j.atmosres.2020.105443, 2021.

Cao, F., Zhang, Y.-X., Zhang, Y.-L., Song, W.-H., Zhang, Y.-X., Lin, Y.-C., Gul, C., and Haque, M. M.: Molecular compositions of marine organic aerosols over the Bohai and Yellow Seas: Influence of primary emission and secondary formation, Atmospheric Research, 297, 107088, https://doi.org/10.1016/j.atmosres.2023.107088, 2024.

Cao, J., Lee, S., Chow, J. C., Watson, J. G., Ho, K., Zhang, R., Jin, Z., Shen, Z., Chen, G., and Kang, Y.: Spatial and seasonal distributions of carbonaceous aerosols over China, Journal of geophysical research: atmospheres, 112, https://doi.org/10.1029/2006JD008205, 2007.

Chen, L.-W. A., Moosmüller, H., Arnott, W. P., Chow, J. C., Watson, J. G., Susott, R. A., Babbitt, R. E., Wold, C. E., Lincoln, E. N., and Hao, W. M.: Emissions from laboratory combustion of wildland fuels: Emission factors and source profiles, Environmental science & technology, 41, 4317-4325, https://doi.org/10.1021/es062364i, 2007.

Chen, W.-C.: Pollution characteristics and source apportionment of ambient particulate matter Pollution in Hangzhou, Yangtze River Delta of China (Chinese), Master's dissertation, Zhejiang: Zhejiang University, https://kns.cnki.net/kcms/detail/detail.aspx?filename=1018085328.nh&dbname=CMFDTEMP, 2018.

Chow, J. C., Watson, J. G., Kuhns, H., Etyemezian, V., Lowenthal, D. H., Crow, D., Kohl, S. D., Engelbrecht, J. P., and Green, M. C.: Source profiles for industrial, mobile, and area sources in the Big Bend Regional Aerosol Visibility and Observational study, Chemosphere, 54, 185-208, https://doi.org/10.1016/j.chemosphere.2003.07.004, 2004.

Engling, G., Lee, J. J., Tsai, Y.-W., Lung, S.-C. C., Chou, C. C.-K., and Chan, C.-Y.: Size-resolved anhydrosugar composition in smoke aerosol from controlled field burning of rice straw, Aerosol Science and Technology, 43, 662-672, https://doi.org/10.1080/02786820902825113, 2009.

Geng, X., Li, J., Zhong, G., Zhao, S., Tian, C., Zhang, Y.-L., and Zhang, G.: Ship Emissions as the Largest Contributor to Coastal Atmospheric Black Carbon at a Receptor Island in Southern China, Environmental Science & Technology Letters, https://doi.org/10.1021/acs.estlett.4c00362, 2024.

Hou, S., Liu, D., Xu, J., Vu, T. V., Wu, X., Srivastava, D., Fu, P., Li, L., Sun, Y., and Vlachou, A.: Source apportionment of carbonaceous aerosols in Beijing with radiocarbon and organic tracers: insight into the differences between urban and rural sites, Atmospheric chemistry and physics, 21, 8273-8292, https://doi.org/10.5194/acp-21-8273-2021, 2021.

Huang, Z.-S., Xiu, G.-L., Zhu, M.-Y., Tao, J., and Yu, J.-Z.: Characteristics and sources of carbonaceous species in $PM_{2.5}$ in summer and winter in Shanghai, Environmental Science & Technology (Chinese), 37(4), 124-129, https://kns.cnki.net/kcms2/article/abstract?v=FCWB7knoBeRkVSj6Unv_6RaC5wbWfztEm-BorFH8uzLyqe2OdII8abo7eMfjsgKp9xKYwtAdUIjtdBknD5Vrj6TcsKzcJt63sJD4SuTPR65I1nL9MFjLnw

YsGbjbTnfIYPhbHNNRLcsNBM3NiHEs5oMs5huq4wP503GxNi03G8_tcAAqx3iHNw==&uniplatform=NZKPT&language=CHS, 2014.

Jung, J., Lee, S., Kim, H., Kim, D., Lee, H., and Oh, S.: Quantitative determination of the biomass-burning contribution to atmospheric carbonaceous aerosols in Daejeon, Korea, during the rice-harvest period, Atmospheric Environment, 89, 642-650, https://doi.org/10.1016/j.atmosenv.2014.03.010, 2014.

Kang, H., Zhu, B., Wang, H.-L., and Shi, S.-S.: Characterization and variation of organic carbon (OC) and elemental carbon (EC) in $PM_{2.5}$ during the winter in the Yangtze River Delta region, China, Environmental Science (Chinese), 39(3), 961-971, https://link.cnki.net/doi/10.13227/j.hjkx.201706178, 2018.

Liang, C.-S., Duan, F.-K., He, K.-B., and Ma, Y.-L.: Review on recent progress in observations, source identifications and countermeasures of $PM_{2.5}$, Environment International, 86, 150-170, https://doi.org/10.1016/j.envint.2015.10.016, 2016.

Liang, L., Engling, G., Cheng, Y., Liu, X., Du, Z., Ma, Q., Zhang, X., Sun, J., Xu, W., and Liu, C.: Biomass burning impacts on ambient aerosol at a background site in East China: Insights from a yearlong study, Atmospheric Research, 231, 104660, https://doi.org/10.1016/j.atmosres.2019.104660, 2020.

Liang, L., Engling, G., Liu, C., Xu, W., Liu, X., Cheng, Y., Du, Z., Zhang, G., Sun, J., and Zhang, X.: Measurement report: Chemical characteristics of $PM_{2.5}$ during typical biomass burning season at an agricultural site of the North China Plain, Atmospheric Chemistry and Physics, 21, 3181-3192, https://doi.org/10.5194/acp-21-3181-2021, 2021.

Liu, H., Wang, Q., Tian, J., Wang, J., Tian, R., Zhang, Y., Zhang, Q., Xue, Y., Xu, H., and Ran, W.: Source-specific mass absorption efficiencies of char-EC and soot-EC improve accuracy in black carbon radiative effect estimation, Journal of Geophysical Research: Atmospheres, 130, e2024JD043079, https://doi.org/10.1029/2024JD043079, 2025.

Mohn, J., Szidat, S., Fellner, J., Rechberger, H., Quartier, R., Buchmann, B., and Emmenegger, L.: Determination of biogenic and fossil CO_2 emitted by waste incineration based on $^{14}CO_2$ and mass balances, Bioresource Technology, 99, 6471-6479, https://doi.org/10.1016/j.biortech.2007.11.042, 2008.

Ren, Y., Wang, G., Tao, J., Zhang, Z., Wu, C., Wang, J., Li, J., Wei, J., Li, H., and Meng, F.: Seasonal characteristics of biogenic secondary organic aerosols at Mt. Wuyi in Southeastern China: Influence of anthropogenic pollutants, Environmental pollution, 252, 493-500, https://doi.org/10.1016/j.envpol.2019.05.077, 2019.

Sang, X., Zhang, Z., Chan, C., and Engling, G.: Source categories and contribution of biomass smoke to organic aerosol over the southeastern Tibetan Plateau, Atmospheric Environment, 78, 113-123, https://doi.org/10.1016/j.atmosenv.2012.12.012, 2013.

Schmidl, C., Marr, I. L., Caseiro, A., Kotianová, P., Berner, A., Bauer, H., Kasper-Giebl, A., and Puxbaum, H.: Chemical characterisation of fine particle emissions from wood stove combustion of common woods growing in mid-European Alpine regions, Atmospheric Environment, 42, 126-141, https://doi.org/10.1016/j.atmosenv.2007.09.028, 2008.

Song, W., Zhang, Y.-L., Zhang, Y., Cao, F., Rauber, M., Salazar, G., Kawichai, S., Prapamontol, T., and Szidat, S.: Is biomass burning always a dominant contributor of fine aerosols in upper northern Thailand?, Environment International, 168, 107466, https://doi.org/10.1016/j.envint.2022.107466, 2022.

Song, W., Zhang, Y., Gao, M., Xie, F., Cao, F., Rauber, M., Kawichai, S., Prapamontol, T., Szidat, S., Peng, Y., Carmichael, G. R., and Zhang, Y.-L.: Biomass burning increase in Southeast Asia is dominated by char black

carbon, Communications Earth & Environment, 7, 359, 10.1038/s43247-026-03431-0, https://doi.org/10.1038/s43247-026-03431-0, 2026.

Stuiver, M. and Polach, H. A.: Discussion reporting of ^{14}C data, Radiocarbon, 19, 355-363, https://doi.org/10.1017/S0033822200003672, 1977.

Szidat, S., Salazar, G. A., Vogel, E., Battaglia, M., Wacker, L., Synal, H.-A., and Türler, A.: ^{14}C analysis and sample preparation at the new Bern Laboratory for the Analysis of Radiocarbon with AMS (LARA), Radiocarbon, 56, 561-566, https://doi.org/10.2458/56.17457, 2014.

Xie, F., Cao, F., Popovicheva, O., Huang, Z.-L., Chichaeva, M., Lin, Y.-C., Song, W.-H., Kovach, R., Zavgorodnyaya, Y., and Wu, C.-L.: Wildfires significantly enhance light absorption of black carbon and brown carbon aerosols in Moscow urban atmosphere, Sustainable Horizons, 17, 100169, https://doi.org/10.1016/j.horiz.2025.100169, 2026.

Xing, J.: Sources and atmospheric processes of atmospheric $PM_{2.5}$ in the Yangtze River Estuary based on experimental component analysis and PMF model (Chinese), Master's dissertation, Shang Hai: East China Normal University, https://link.cnki.net/doi/10.27149/d.cnki.ghdsu.2022.004027, 2022.

Xiong, X., Zhou, W., Hou, X., Cheng, P., Du, H., Zhao, X., Wu, S., Hou, Y., Lu, X., and Fu, Y.: Time series of atmospheric $\Delta^{14}CO_2$ recorded in tree rings from Northwest China (1957-2015), Chemosphere, 272, 129921, https://doi.org/10.1016/j.chemosphere.2021.129921, 2021.

Yang, X. Y., Cao, F., Lin, Y. C., Fan, M. Y., Wu, C. L., Yu, M. Y., Song, W. H., and Zhang, Y. L.: Distinct sources of char and soot black carbon aerosols during winter haze at pair sites in north China: Source apportionment from dual-carbon isotope constrained PMF, Journal of Geophysical Research: Atmospheres, 130, e2024JD043077, https://doi.org/10.1029/2024JD043077, 2025.

Ye, Z.-L., Liu, J.-S., Li, Q., Ma, S.-S., and Xu, P.: Characteristics and source identification of carbonaceous aerosols in $PM_{2.5}$ measurements during summer and fall in Changzhou, Environmental Science (Chinese), 38(11), 4469-4477, https://link.cnki.net/doi/10.13227/j.hjkx.201704295, 2017.

Zhao, Z., Cao, J., Shen, Z., Huang, R.-J., Hu, T., Wang, P., Zhang, T., and Liu, S.: Chemical composition of $PM_{2.5}$ at a high-altitude regional background site over Northeast of Tibet Plateau, Atmospheric Pollution Research, 6, 815-823, https://doi.org/10.5094/APR.2015.090, 2015.

Zong, Z., Wang, X., Tian, C., Chen, Y., Fu, S., Qu, L., Ji, L., Li, J., and Zhang, G.: PMF and PSCF based source apportionment of $PM_{2.5}$ at a regional background site in North China, Atmospheric Research, 203, 207-215, https://doi.org/10.1016/j.atmosres.2017.12.013, 2018.